University of Alberta

Excitation of Ultrasonic Guided Waves In Bone Plates Using A Phased Array System

by

Kim-Cuong Thi Nguyen

A thesis submitted to the Faculty of Graduate Studies and Research in partial fulfillment of the requirements for the degree of

Master of Science

Medical Sciences - Radiology and Diagnostic Imaging

Fall 2013
Edmonton, Alberta

Abstract

Ultrasonic guided waves have been exploited to study long bones using the axial transmission technique. The application of phased array (PA) technology to bone study is uncommon and the conventional technique involves the employment of a pair of angled beam transducers, which is laborious. In this thesis, we investigated the use of a commercial non-medical ultrasonic PA system to study Lamb waves in Plexiglas and bovine bone plates using a single array probe and two array probes. Data acquired by the single probe was deteriorated by the presence of crosstalk. We developed a Radon-based adaptive crosstalk cancellation algorithm to remove the crosstalk and recover the signals. Using the two array probes, we studied beam steering to preferentially excite guided modes for bone assessment. The results have demonstrated the advantages of the PA system over the conventional single-emitter-single-receiver system in terms of accuracy, speed, and patient comfort, if used in clinical settings.

Acknowledgements

First and foremost, I would like to thank my parents, brother, and beloved people for their support and encouragement throughout my studies. I missed them very much for the past two years when I was away from home.

I would like to express my deepest gratitude to my supervisors for giving me the freedom to develop my own ideas. I gratefully appreciate Dr. Lawrence Le for his enthusiasm in research, his creative ideas, and his critical and useful comments on my thesis project, presentations, and writings. I also thank my co-supervisor, Dr. Edmond Lou for giving me an opportunity to participate in the clinical scoliosis ultrasound project and guiding me throughout my studies.

I would like to thank Drs. Mauricio Sacchi and Jeffrey Gu, from whom I learnt enthusiastically about signal processing and wave propagation. Also, I sincerely thank Dr. Larry Filipow for his critical comments on my thesis.

I thank all my colleagues: Dr. Rui Zheng, Wei Chen, Tho Tran, Quang Vo, and Duc Nguyen. They all together created an enjoyable and stimulating working environment. I really appreciate Ms. Joanne Houtstra and Ms. Lynda Loiseau for their kind assistance in administration matters.

Last but not the least, I want to thank the Vietnam Ministry of Education and Training, Faculty of Medicine and Dentistry, Department of Radiology and Diagnostic Imaging, and Women's and Children's Health Research Institute for financially supporting my graduate research.

Table of Contents

1 Introduction **1**

1.1 Background of Osteoporosis 1

1.2 Current Techniques to Evaluate Osteoporosis 5

1.2.1 Ionizing Radiation Based Methods 5

1.2.2 Non-radiation Based Methods 9

1.3 Quantitative Ultrasound Techniques 11

1.3.1 Pulse-Echo Technique 11

1.3.2 Transverse Transmission Technique 12

1.3.3 Axial Transmission Technique 14

1.3.4 Recent Application of Linear Array Transducer System to Study Bone Tissues 15

1.4 Guided Waves and Their Application in the Study of Bone Tissues 17

1.5 Objectives of the Thesis 20

1.6 Organization of the Thesis 21

2 Excitation of Ultrasonic Waves Using A Phased Array System with A Single Array Probe **23**

2.1 Phased Array System 24

2.1.1 TomoScan FOCUS LT ^{TM} Ultrasound Scanner 24

2.1.2 Data Acquisition 26

2.1.3 Resolution Measures 29
2.1.3.1 Near Field Length 29
2.1.3.2 Axial Resolution 29
2.1.3.3 Lateral Resolution 30
2.2 The Linear $\tau - p$ Transform 31
2.3 Adaptive Crosstalk Cancellator 34
2.3.1 Adaptive Crosstalk Cancellator 34
2.3.2 Validation of Adaptive Crosstalk Cancellator 36
2.4 Applications 41
2.4.1 24-mm Thick Plexiglas plate 41
2.4.2 9-mm Thick Plexiglas plate 45
2.4.3 6-mm Thick Bovine Bone Plate 47
2.5 Concluding Remarks 47

3 Excitation of Guided Waves by Beam Steering Using Two Array Probes* **50**

3.1 Materials and Methods 52
3.1.1 Preparation of Samples 52
3.1.2 Data Acquisition 53
3.2 Source Influence Theory: Excitation Function 56
3.3 Results and Discussion 57
3.3.1 Brass Plate 57
3.3.2 Bovine Bone Plate 63
3.3.3 Excitation Function 66
3.4 Concluding Remarks 68

4 Conclusions and future directions **70**

Bibliography **74**

Appendix A Effective Aperture Angle **83**

List of Tables

3.1 Parameters used to simulate dispersion curves for the brass plate and bone plate. The compressional wave velocity (v_p) and shear wave velocity (v_s) of the brass plate were taken from Table A-2 of Olympus NDT (2010) while the density (ρ) was measured. The v_p, v_s, and ρ of the bone plate were taken from Dodd et al. (2006) while the attenuation coefficients, α_p and α_p were from Le et al. (2010a). We also measured the v_p of the brass and bone plates and the measurements were 4.56 km/s and 4.09 km/s respectively, which are very close to the the reported values in the literature (Olympus NDT, 2010; Dodd et al., 2006). 60

3.2 Parameters for the -9 dB phase velocity bandwidth for five steering angles. The c_{p1}^{-} and c_{p2}^{-} refer to the phase velocities ($< c_o$) of the peaks of the first and second sidelobes. 68

List of Figures

1.1 Bone classifications based on shape (TCHS Sports Medicine ROP, 2013). 2

1.2 Bone structure with two main forms: cortical bone and trabecular bone (The Altanta Equine Clinic, 2013) 2

1.3 Normal bone versus osteoporotic bone (INNOVATE R&D, 2013) 3

1.4 A schematic diagram of a pulse-echo measurement showing an echo backscattered by the internal cancellous bone structure. . 11

1.5 A schematic diagram of the transverse transmission measurement technique. 13

1.6 Process flow sheet 14

1.7 The deformation of particle planes and the retrograde elliptical motion at the plate surface of the A_0 and S_0 modes (Wenzel, 1992). 19

2.1 Possible crosstalk in an array probe. 24

2.2 The ultrasound phased array system: (a) The TomoScan FOCUS LT^{TM} phased array acquisition system (1), the Windows XP-based computer with the TomoView^{TM} software to control the acquisition process (2), and the probe unit (3). (b) the 64-element phased array probe. 25

2.3 (a) The dimensional parameters of an array transducer: $p-$the pitch, $e-$the elevation, and $A-$the aperture. (b) An illustration of the principle of beam steering by delaying the firings of the elements successively (modified from Olympus NDT (2007)). . 27
2.4 The phantom experiment with the 64-element array probe on a 9-mm thick Plexiglas plate. 28
2.5 The *in vitro* experiment with the 64-element array probe on a 6-mm thick bovine bone plate. 28
2.6 A schematic diagram of axial resolution of the beam (modified from Olympus NDT (2007)). 29
2.7 A schematic diagram of lateral resolution of the beam (modified from Olympus NDT (2007)). 30
2.8 The schematic diagram for forward and inverse linear τ-p transform. The records are summed along straight lines with different slopes, p and time intercepts, τ. Stacking along p_1 goes through strong peaks of the records and thus yields a strong amplitude focus in the τ-p panel (dark gray ellipse) while stacking along p_2 encounters amplitudes of opposite polarities and thus leads to less Radon energy. Stacking along p_3 leads to trivial Radon energy due to very small amplitudes of the signals (modified from Gu and Sacchi (2009)). 32
2.9 Principle of adaptive crosstalk cancellator(Widrow et al., 1975). 35

2.10 A noiseless example shows the simulated and ACC-filtered crosstalk and signals with their corresponding $\tau - p$ panels. (a) The simulated reference crosstalk; (b) The simulated data consisting of signals (A and B) and crosstalk (C and D) where the amplitudes of the latter are only half of those of the reference crosstalk; (c) The predicted crosstalk; (d) The ACC-filtered signals. 37
2.11 Comparison between the ACC-filtered (red) and simulated (black) data at 17.25 mm offset. 38
2.12 The MSE between the signal and filtered signal for different values of step-size β and filter length L. 39
2.13 A noisy example shows the simulated and ACC-filtered crosstalk and signals with their corresponding $\tau - p$ panels. The SNR is 10 dB. (a) The simulated reference crosstalk; (b) The simulated data consisting of signals (A and B) and crosstalk (C and D) where the amplitudes of the latter are only half of those of the reference crosstalk; (c) The predicted crosstalk; (d) The ACC-filtered signals. 40
2.14 Comparison between the ACC-filtered (red) and noisy (black) data at 17.25 mm offset. 41
2.15 The reference crosstalk plotted in three different domains: (a) $(t-x)$, (b) $(\tau-p)$, and (c) $(f-c)$. The letters A, B, and C denote the three different arrivals existing in the transducer array, which correspond to the direct wave, guided waves propagating in the matching layer, and reflection arrivals (refer to Fig. 2.16 for further details). 42
2.16 Crosstalk inside an array transducer. 43

2.17 The crosstalk-corrupted data for the 24-mm thick Plexiglas plotted in three different domains: (a) $(t-x)$; (b) $(\tau-p)$ and (c) $(f-c)$. 44

2.18 The crosstalk-filtered signals for the 24-mm thick Plexiglas using three approaches: (a) the conventional ACC in $(t-x)$, (b) normal subtraction in $(\tau-p)$, and (c) ACC in $(\tau-p)$. The results are represented in three different panels ($(t-x)$, $(\tau-p)$, and $(f-c)$) for verification. 45

2.19 Crosstalk removal in a 9-mm thick Plexiglas: (a) the original data, (b) the data after multiple reflections are muted in the $\tau-p$ domain, and (c) the ACC-filtered signal. 46

2.20 Crosstalk removal for the 6-mm bovine bone plate: (a) the original data, (b) the data after multiple reflections are muted in the $\tau-p$ domain, and (c) the ACC-filtered signal. 48

3.1 The 6.5-mm thick bovine bone plate. 52

3.2 The ultrasound phased array system: (a) The TomoScan FOCUS LT^{TM} phased array acquisition system (1), the Windows XP-based computer with the TomoView^{TM} software to control the acquisition process (2), and the probe unit (3). (b) The housing with the 16-element and 64-element probes. The P16 was the transmitter array while the P64 was the receiver array. 54

3.3 A cross-section of the experiment setup. The housing hosted two ultrasound probes in place: a 16-element (P16) probe as the transmitter and a 64-element probe as the receiver. The probes rested on the ultrasound gel pads, which acted as coupling media. The pads then overlaid the plate. Only one group (five elements) in P16 was used as source generator and 60 groups in P64 as receivers. The receivers were steered at the same inclination as the transmitting beam to enhance the receiving sensitivities to propagating guided waves with phase velocity, c_o related to the inclination, θ_i by Snell's law, $\sin\theta_i = v_w/c_o$ where v_w was the velocity of the coupling medium. 55

3.4 The normalized excitation spectra for six different steering angles. The velocity value shown above each figure is the phase velocity determined by Snell's law (Eq. (3.1) in the text). The phase velocity determined by Snell's law is denoted by c_o; The phase velocities, c_o^- and c_o^+, are defined at the values of $|F|$ equal to -9 dB of the maximum; The c_{p1}^- and c_{p2}^- refer to the phase velocities ($< c_o$) of the peaks of the first and second sidelobes. 58

3.5 The time-offset data for the brass plate at six different incident angles: (a) 0°, (b) 20°, (c) 30°, (d) 40°, (e) 50°, and (f) 60°. . . 59

3.6 The dispersion panels of the brass plate data for the six different steering angles: (a) 0°, (b) 20°, (c) 30°, (d) 40°, (e) 50°, and (f) 60°. Superimposed are the theoretical dispersion curves. The c_o, c_o^-, c_o^+, c_{p1}^-, and c_{p2}^- are referred to Fig. 3.4 for their definitions. 61

3.7 The time-offset data for the bone plate at six different incident angles: (a) 0°, (b) 20°, (c) 30°, (d) 40°, (e) 50°, and (f) 60°. . . 64

3.8 The dispersion panels of the bone plate data for six different steering angles: (a) 0°, (b) 20°, (c) 30°, (d) 40°, (e) 50°, and (f) 60°. Superimposed are the theoretical dispersion curves. The c_o, c_o^-, c_o^+, c_{p1}^-, and c_{p2}^- are referred to Fig. 3.4 for their definitions. 65

4.1 The dispersion panels of a human tibia data set for five different incident angles: 0°, 20°, 30°, 40°, and 60°. 73

A.1 Diagram used to determine the effective aperture angle, β. AB represents the aperture of a group of elements used as emitter. 83

List of Abbreviations

ACC	*Adaptive crosstalk cancellator*
ANC	*Adaptive noise cancellator*
BMD	*Bone mineral density*
BUA	*Broadband ultrasound attenuation*
DXA	*Dual X-ray absorptiometry*
FAS	*First arriving signal*
FT	*Fourier transform*
GW	*Guided wave*
HU	*Hounsfield unit*
MRI	*Magnetic resonance imaging*
MSE	*Mean-squared-error*
NDT	*Nondestructive testing*
PA	*Phased array*
pQCT	*Peripheral quantitative computed tomography*
QCT	*Quantitative computed tomography*
μCT	*Micro computed tomography*
QUS	*Quantitative ultrasound*
RT	*Radon transform*
SESR	*Single emitter single receiver*
SD	*Standard deviation*

SIT	*Source influence theory*
SPA	*Single photon absorptiometry*

Chapter 1

Introduction

1.1 Background of Osteoporosis

Bone

Bones hold significant functions in our bodies such as structural framework, body movement, mechanical support, vital organ protection, mineral storage, and blood cell production. Based on the shape (Fig. 1.1), the bones can be classified into six types: long bone (e.g humerus, tibia, femur, radius), short bone (carpal and tarsal), flat bones (parietal bone, hip bone, rib), irregular bones (vertatebra, sacrum), sesamoid bones (patella), and sutural bones (Ivy-Rose Holistic, 2013).

The skeleton is comprised of two forms of bone tissues: cortical (compact) and trabecular (cancellous or spongy) bones (Fig. 1.2). The cortical bone occupies 70–80% bone mass, almost four times the mass of trabecular bone (Blake et al., 1999). In macroscopic view , the cortical bone is very compact and dense. In fact, it contains a system of nerves, blood vessels, and osteons, a basic structural unit of compact bone. For cancellous bone, the structural unit is trabecula which is organized in a three-dimensional lattice network. The spaces between trabeculae are filled with fat and marrow (Njeh, 1999).

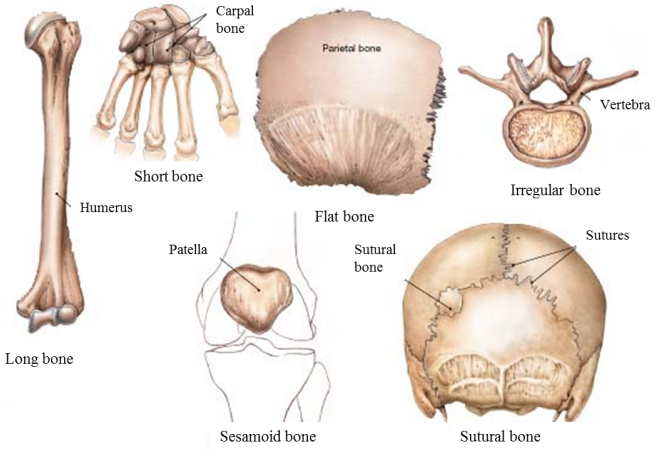

Figure 1.1: Bone classifications based on shape (TCHS Sports Medicine ROP, 2013).

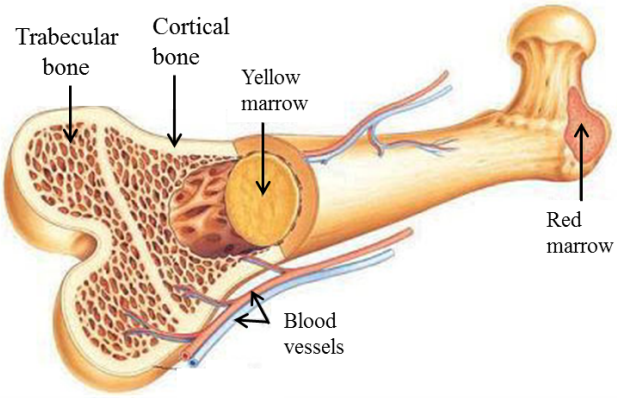

Figure 1.2: Bone structure with two main forms: cortical bone and trabecular bone (The Altanta Equine Clinic, 2013)

Osteoporosis

Osteoporosis is a systemic skeletal disease characterized by gradual loss of bone density, micro-architectural deterioration of bone tissue, and thinning of the cortex, leading to bone fragility and an enhanced risk of fractures (WHO Scientific Group, 2004). Osteoporotic bone has the same anatomical bone volume but has lower bone tissue volume and higher fat than normal bone. Thus, the diseased bone shows cortical thinning and porosis (Blake et al.,

1999) as shown in Fig. 1.3. Cortical thickness measurement in long bones has been investigated for the incidence of osteoporosis. Loss of cortical bone involves an increase of intracortical porosity due to trabecularization of cortical bone (Bousson et al., 2001; Zebaze et al., 2010) and cortical thinning due to the expansion of marrow cavity on the endosteal surface (Langton and Njeh, 2003).

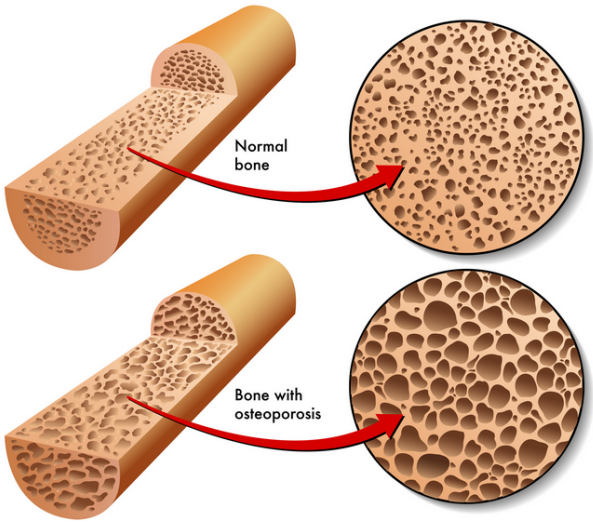

Figure 1.3: Normal bone versus osteoporotic bone (INNOVATE R&D, 2013)

Osteoporosis is often known as a silent enemy because bone loss occurs without symptoms. The victims may not know they have osteoporosis and when the disease is in its advanced stages, damage is severe. For example, a fall may cause a hip to fracture or a vertebra to collapse. Osteoporosis is mainly caused by an imbalance between bone formation and bone resorption. This is largely due to a net loss of calcium in the body. Resorption leads to thinning of the cortical bone layer and the trabeculae, which decreases the strength and connectivity of bone micro-architecture (Bartl and Frisch, 2009; Turner, 2002). These factors lead to degraded bone quality and enhanced

fracture risk.

It is estimated that more than 8.9 million fractures are caused by osteoporosis worldwide each year, which amounts to one osteoporotic fracture every 3.5 seconds. The fragility-fracture rates, for people over 50, are 1 in 3 for women and 1 in 5 for men. Although women have higher osteoporotic fracture ratio than men, the risk of fracture-related mortality is higher in men than in women (International Osteoporosis Foundation, 2013). In Canada, there are about 30,000 patients with hip fracture annually and among them, 28% of females and 37% of males die within a year. The cost of osteoporosis and related fractures was about $7.7 billion in 2012 as reported by the Osteoporosis Canada organization (Osteoporosis Canada, 2013). By the year 2050, the occurrence of osteoporotic hip fractures in Asia is expected to increase and be responsible for 50% of all fractures worldwide. In Vietnam, osteoporosis affects over 2.8 million people and related hip fractures are projected to reach more than 30,000 in 2020 and 47,000 in 2050 (International Osteoporosis Foundation, 2013; Hien et al., 2005).

The societal burden of osteoporosis is difficult to comprehend because it includes monetary cost and non-monetary cost. The monetary cost is associated with hospital and rehabilitative care, long-term health care, and medication. The non-monetary cost is mainly related to the influential factors on the quality of life such as pain, immobility, poor medical state, emotions, and daily-life dependency. Osteoporosis may lead to some health consequences such as mobility impairment and decreased ability to perform normal daily activities independently. Therefore, a negative impact upon the emotions of the patients such as anxiety, depression, and loss of self-confidence is possible.

1.2 Current Techniques to Evaluate Osteoporosis

The techniques to assess osteoporosis can be classified into categories:

- *Ionizing radiation based methods:* These mainly include single photon absorptiometry (SPA), single X-ray absorptiometry (SXA), dual-energy X-ray absorptiometry (DXA or DEXA), radiography, and quantitative computed tomography (QCT).

- *Non-Ionizing radiation based methods:* These mainly include magnetic resonance imaging (MRI) microscopy and quantitative ultrasound (QUS) techniques.

1.2.1 Ionizing Radiation Based Methods

Bone mineral density (BMD) measurement is the most widely adopted quantitative diagnostic assessment of osteoporosis (World Health Organization, 2004). BMD is calculated by dividing the amount of mineral in the specific bone site scanned by the scan area or volume. The units are expressed as areal BMD (g/cm^2) or volumetric BMD (g/cm^3). The BMD values at the site are compared to young healthy reference means and expressed in standard deviation (SD) units, known as T-scores. T-score is a relevant measure for osteoporosis screening. When T-score ≥ -1 SD, the BMD is considered normal. Patients are diagnosed with osteoporosis when their T-score ≤ -2.5 SD (WHO Scientific Group, 2004).

The first BMD measurement was performed by SPA (Cameron and Sorenson, 1963). The nature of the method is based on the attenuation of a monochromatic photon beam from a single-energy radionuclide source as it

passes through bone. The attenuation of the photon beam through bone tissue depends on the density and thickness of the bone and can be calculated by the incident and transmitted intensities of the photon beam. However, in $in-vivo$ application, the attenuation of the photon beam is affected not only by the bone but also by the soft tissue. The soft tissue can be fat, muscle, and skin, the thickness of which is unknown. To remove the effect of soft tissue, the anatomical site is immersed in a soft tissue equivalent material such as water to keep the total thickness through bone and soft tissue unchanged. The relevant equations to calculate bone areal density can be solved to obtain the areal bone density (Langton and Njeh, 2010). This method estimates cortical and trabecular bone mass combined *in vivo*, usually of the appendicular sites, such as the heel, wrist, radius, metacarpals, or phalanges. However, the SPA has some limitations. The photon source is a radionuclide, which needs replacement. There are artifacts due to source decay and a long scanning time is required due to low photon fluence. The SXA employs the same physical principles as SPA except that the radionuclide source is replaced by an X-ray tube. The use of an X-ray source results in controllable and stable source strength with time, better image resolution, and faster scanning speed (Kelly et al., 1994). Recently, DXA has been developed to measure BMD precisely using two X-ray beams with different energies to replace the water bath. When the energies of the two beams differ, the effect of the soft tissue can be removed and attenuation due to skeletal tissues is accurately estimated. The BMD measured by this technique has been used widely for bone assessment to predict the bone strength in human vertebrae (Perilli et al., 2012); to study the fracture identification in women with vertebral or low trauma fracture (Krueger et al., 2013); and to investigate the beneficial effects of physical

activity in primary school on children's bone mass (Meyer et al., 2013).

Radiography has also been used to evaluate cortical thinning due to osteoporosis. The osteoporotic subjects have a thinner cortex than normal people (Werner, 2005). The ratio of cortical thickness to the total width or the ratio of cortical area to the total cross-sectional area were found to be good indicators of osteoporosis (WHO Scientific Group, 2004). Barnett and Nordin (1960) developed different score measures from radiographs to diagnose osteoporosis. Bloom (1980) used the cortical bone thickness of the distal end of left humerus measurements from antero-posterior radiographs to estimate bone loss for osteoporosis in women. Recently, Mather et al. (2013) demonstrated a strong correlation between proximal humeral cortical bone thickness measured from antero-posterior shoulder radiographs and BMD measured by DXA in an *in vivo* study for osteoporosis diagnosis.

In addition to these techniques, QCT is a method to measure volumetric bone mineral density (g/cm^3), which is converted from Hounsfield units (HU). The HU scale, $HU_T = 1000 \times (\mu_T - \mu_w)/\mu_w$, is computed by comparing the linear attenuation coefficients of the tissue (μ_T) and distilled water (μ_w) at standard pressure and temperature. The HU scale is linear with air being -1000, water 0, and bone ranging from 300 - 3000 units. QCT is considered a high resolution and excellent contrast technique for bone imaging because of the strong difference in attenuation coefficients between bone and surrounding soft tissues (Langton and Njeh, 2010). Miyabara et al. (2012) showed a good comparison between the volumetric BMD measured from QCT and the area BMD computed from DXA for osteoporosis risk estimation in menopausal women. Gruber et al. (2013) used QCT to calculate the BMD of the proximal femur and found that the measurements in the femur might discriminate the

osteoporotic fracture patients from the non-fractured patients. In the assessment of cancellous bone density, one advantage of QCT over DXA is that the former measures the true volumetric BMD, not an areal BMD (WHO Scientific Group, 2004).

There are two main types of QCT systems, namely peripheral quantitative computed tomography (pQCT) and micro computed tomography (μCT). pQCT is typically utilized to measure the volumetric bone density of the peripheral skeleton while μCT is designed for imaging the trabecular micro structure. The pQCT scanner includes an X-ray source and an array of detectors. The source-detector assembly can be moved in axial and transverse directions or rotated arround the subject by a mechanical system. Louis et al. (1995) showed that pQCT had a high accuracy to assess cortical thickness of the left forearm in a population of 30 cadavers. Augat et al. (1996) also used pQCT to study bone strength at the radius and femoral neck of 20 cadavers and found a high correlation between the geometrical properties (cross-sectional area, mean thickness, moment of inertia) and the fracture load at these skeletal sites. Nishiyama et al. (2010) found that the cortical thicknesses at distal radius and tibia in postmenopausal women with osteopenia were found to be thinner than those of normal women in an *in vivo* study using pQCT.

Different from pQCT, μCT is a radioscopic modality, which uses a microfocus X-ray tube as a source, an image intensifier, and a cone-beam reconstruction algorithm to create a three-dimensional image. In addition, the X-ray source and detectors in a μCT are stationary while the specimen is rotated about a single axis. X-ray photons from the source are transmitted through the sample and detected by a planar image intensifier at each rotation. A volumetric image of the sample is reconstructed from a series of planar

images. Müller and Rüegsegger (1996) used μCT to image trabecular micro-architecture *in vitro* and used finite element modeling to evaluate the effects of anisotropy and density on bone strength.

SPA, SXA, DXA, and QCT are important modalities in providing valuable BMD information and QCT provides in addition the volumetric shape and macro-architecture of bone tissue. However, they involve radiation exposure to the patients and the BMD measurements alone do not provide elasticity of bone tissue, which is an important parameter to bone quality.

1.2.2 Non-radiation Based Methods

Magnetic resonance imaging (MRI) is a non-destructive, non-invasive, and non-ionizing method to reconstruct a three-dimensional bone image. The method is based on the application of high magnetic fields, transmission of radio frequency waves, and detection of radio frequency signals from the excited hydrogen protons. The imaging principle of MRI makes use of the difference in water content between bone and soft tissues. The bone minerals within the cortical and trabecular bone have low water content and thus lack free protons while the soft tissue and marrow yield strong signals because they have abundant free protons. Due to the difference in free protons available for imaging bone and soft tissues, MRI is able to image bone tissues for bone quality assessment.

Link et al. (1998) applied texture analysis to study MRI images of the calcaneus in 50 females (23 postmenopausal patients with osteoporotic hip fractures and 27 postmenopausal controls) and found that the morphological features (trabecular thickness, trabecula numbers, trabecular spacing, trabecular bone area fraction, etc) could differentiate between postmenopausal women

with and without osteoporotic hip fractures. Majumdar et al. (1996) found the trabecular parameters measured from the reconstructed MRI images of human distal radius cubes contributed to the prediction of bone strength and elasticity. Vieth et al. (2001) compared standard morphological trabecular parameters of 30 calcaneus specimens using MRI images and radiographs. Their study showed that the MRI derived parameters were strongly correlated with those obtained from radiographs. Though MRI delivers no ionizing radiation, the scanner is very bulky, complicated, and expensive, not to mention hard to get access to.

Recently, quantitative ultrasound (QUS) has gained considerable attention on the study of osteoporosis. Ultrasound uses mechanical waves to probe bone properties and is able to provide bone elasticity information. As well, QUS is ionizing radiation-free, more portable, and economically low-cost. These properties differentiate ultrasound from other conventional methods. The parameters of ultrasound waves such as velocity and attenuation are strongly dependent on the density, geometry (cortical thickness, fractures), and mechanical properties (elasticity or stiffness) of bone. The interactions of ultrasound with bone tissues are very complicated and our understanding of the mechanism is still limited. Langton et al. (1984) provided the first scientific evidence that ultrasound attenuation between osteoporotic and healthy subjects were different. This study opened a new avenue for the use of ultrasound to study osteoporosis.

There are three braodly different methods in the use of QUS to study bone tissue. They are pulse-echo, transmission-through, and axial transmission techniques.

1.3 Quantitative Ultrasound Techniques

1.3.1 Pulse-Echo Technique

The pulse-echo technique uses a single transducer, which acts as an emitter as well as a receiver. When an ultrasound pulse propagates into the tissue and encounters an interface, partition of energy occurs. A portion of the ultrasound energy is transmitted across the interface while the remaining portion is reflected at the interface and returns to the transducer as an echo (Fig. 1.4). Multiple echoes can be generated as well. The average ultrasound velocity of

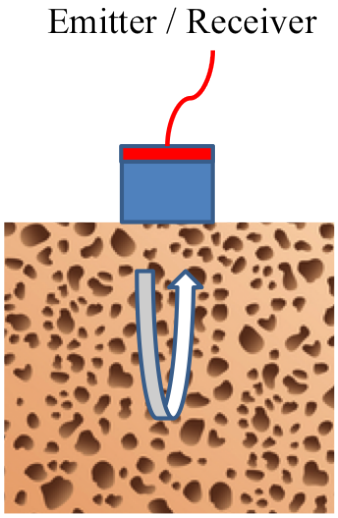

Figure 1.4: A schematic diagram of a pulse-echo measurement showing an echo backscattered by the internal cancellous bone structure.

the medium, v can be calculated by the medium thickness, d and propagation time, t as

$$v = d/2t \tag{1.1}$$

where the denominator "2" takes into account the two-way travel time of the ultrasound beam.

Zheng et al. (2009) used pulse echoes and multiple reflections to estimate cortical attenuation of bovine bones. Zhang et al. (2013) studied the ultrasonic backscattered signals in neonates and found significant correlations between the backscatter coefficient and gestational age, birth weight, and length at birth, and suggested the use of a backscatter coefficient to assess bone status of neonates.

1.3.2 Transverse Transmission Technique

The technique is also known as the transmission-through method and involves two transducers: one acting as an emitter and the other a receiver, placed at opposite sides of the sample (Fig. 1.5). We use the terms, emitter and transmitter, interchangeably in this thesis. Two signals are recorded without and with the sample in the ultrasound beam path. The former is a reference signal through water and the latter is a signal through the sample. The speed of sound of the sample, v_{sample} can be determined by the substitution method (Le, 1998; Zhang et al., 2011)

$$v_{sample} = \frac{L}{L/v_{water} + \Delta t} \tag{1.2}$$

and

$$\Delta t = t_{sample} - t_{water} \tag{1.3}$$

where L is the thickness of the sample, v_{water} is the velocity of sound in water, and t_{water} and t_{sample} are the times of flight of the signals in water without and with the sample respectively. When absorption exists, the traveling speeds through the sample depend on frequency, also known as phase velocities (Sachse and Pao, 1978)

$$c(\omega) = \frac{\omega L}{\omega L/v_{water} + \Delta\varphi(\omega)} \tag{1.4}$$

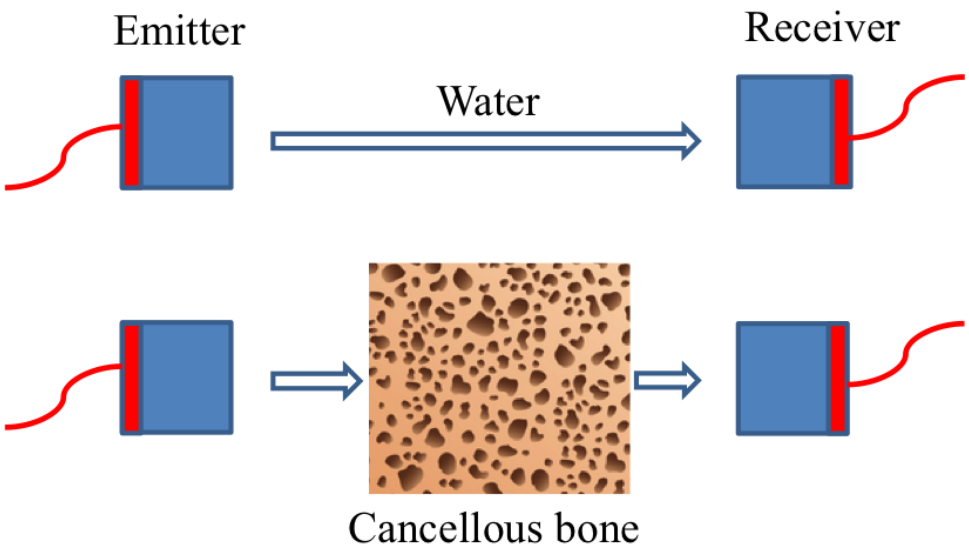

Figure 1.5: A schematic diagram of the transverse transmission measurement technique.

where ω is the angular frequency and $\Delta\varphi(\omega)$ is the unwrapped phase difference between the sample and reference spectra. Dispersion is described by the slope of the linear least-squares regression line fitted to the phase velocity-versus-frequency data within the same frequency range.

Ultrasound experiences loss of energy as it propagates through a sample. The loss is mainly due to scattering, absorption, and transmission, and can be described by the attenuation coefficient, α (in dB/cm) (Zhang et al., 2011)

$$\alpha(\omega) = \frac{20}{L} \ln \frac{|A_{ref}(\omega)|}{|A_{sample}(\omega)|} \tag{1.5}$$

where $A_{ref}(\omega)$ and $A_{sample}(\omega)$ are the spectra of the reference and sample signals. Equation (1.5) does not take into account the transmission loss at the interface.

The transverse transmission principles have found applications in many medical ultrasound bone densitometers (Haney and OBrien, 1986) such as ACHILLES by General Electric, SAHARA by Hologic, and PEGASUS Smart

by DMS. Also in basic research, the principles have been widely used to study the dispersion and attenuation characteristics of bone samples (Wear, 2000; Lee and Choi, 2007) and aluminum foams (Ji et al., 1998; Le et al., 2010b; Zhang et al., 2011).

1.3.3 Axial Transmission Technique

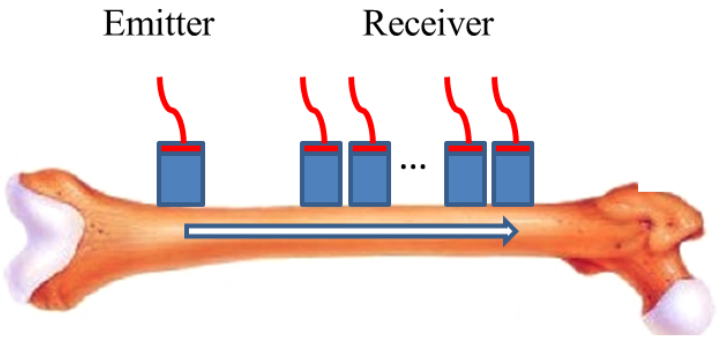

Figure 1.6: A schematic diagram of the axial transmission measurement technique. The emitter is fixed while the receiver moves away from the emitter at uniform spacing intervals.

The axial transmission method is specifically designed to study the mechanical properties of long bones (Lowet and VanderPerre, 1996; Ta et al., 2006; Moilanen et al., 2007; Le et al., 2010a). The technique was originally used more than forty years ago to monitor fractures by measuring the speed of ultrasound across the fracture sites (Siegel et al., 1958; Gerlanc et al., 1975).

During data acquisition, the emitter and the receiver are deployed on the same side of a bone sample. (Fig. 1.6). The emitter is stationary while the receiver is positioned collinearly at locations on one side of the emitter. The receiver's locations are usually evenly spaced and the source-receiver distance is denoted as an offset. The acquisition can be done using a single receiver

measured at multiple locations (Ta et al., 2006; Le et al., 2010a) or a transducer array (Sasso et al., 2006; Minonzio et al., 2010b, 2011b). Therefore the data are acquired at a uniform spatial spacing interval with limited aperture. The recorded signals form a time-offset $(t - x)$ matrix of signal amplitudes. The data records the particle motions of the internal structure subject to the excitation of a vibration and exhibits time history of complex wavefields. The time records show a mixture of high-frequency and high-velocity bulk waves (Le et al., 2010a) and low-frequency and low-velocity surface or guided waves (Muller et al., 2005; Minonzio et al., 2011a; Tran et al., 2013b).

1.3.4 Recent Application of Linear Array Transducer System to Study Bone Tissues

Although a pair of transducers is still the most common means to acquire bone data, an ultrasound array system has recently been used in an axial transmission bone study. The array system or multi-transmitter-multi-receiver system has many advantages over a single-transmitter-single-receiver system. The former has better resolution because of the smaller element footprint, fast acquisition speed, accurate coordination of the receivers, and less motion-related problems. With a phased array (PA) system, beam steering is possible, which is one of my research activities in this thesis.

Bossy et al. (2004a) developed two 1-MHz and 2-MHz linear array probes with two groups of emitters located on opposite sides of a single group of 14 receivers. The method employed the bidirectional transmission of ultrasonic waves along cortical bone and measured the difference in times of flight at adjacent receivers to estimate the compressional wave speed through the cortex without recourse to any property information (velocity, thickness) relevant to

the overlying soft tissue. Bossy et al. (2004b) further applied the technique to extract the compressional wave speeds in 39 excised human radii and found the wave speed was sensitive to both porosity and tissue mineralization in the periosteal region of the cortex. Talmant et al. (2009) used the bidirectional technique to measure the velocity of first arriving signal (FAS) at the one third distal radius location in a subject group consisting of of 122 postmenopausal women without history of fracture and 44 postmenopausal patients with osteoporotic fractures. They found the velocity of FAS discriminated patients with osteoporotic fracture from non-fractured subjects. Moilanen et al. (2013) applied the bi-directional technique with a 0.4 MHz array probe to measure cortical velocity in a subject group of 95 Finnish postmenopausal women (age 45 to 88 years) with and without fracture history. They found that the measured FAS velocity discriminated the fractured subjects from the non-fractured ones equally or better than pQCT and DXA. Sasso et al. (2009) used Bossy's data set (Bossy et al., 2004b) to analyze the energetic late arrival, which is in the guided-wave regime, and found the velocity was highly correlated to cortical layer thickness. The Paris group (Minonzio et al., 2010a,b) developed further linear array probes to study aperture effects on the resolution of the dispersion trajectories of the guided waves, and the soft tissue effects (Chen et al., 2012a). In these studies, they also applied singular value decomposition technique to improve the resolution of the dispersion map of the guided modes.

1.4 Guided Waves and Their Application in the Study of Bone Tissues

Ultrasonic guided waves have seen many successful industrial applications in non-destructive testing (NDT), evaluation, and inspection. Guided wave testing technologies have been applied to material inspection, flaw detection, material characterization, and structural health monitoring (Rose, 2004a). Ultrasonic guided waves have found recent applications in bone study in the past decade.

Surface or guided waves (GWs) require a boundary or structure for their existence. Their propagation is restricted to the near surface or within the structure. These waves are excited by the interaction of elastic waves (compressional and shear) with the boundaries. For GWs within a plate, waves are multiply reflected at the boundaries with mode conversions. The boundaries are strong reflectors (bone/air, bone/soft-tissue or bone/marrow) and act as waveguides. The waveguide traps ultrasound energy within the plate, facilitates multiple reflections, and also guides the wave propagation; the waveguide also retains the guided-wave energy and keeps it from being spread out, thus allowing the guided waves to travel over long distances within the plate (Lowe, 2002). The plate vibrates in different vibration modes, which are known as guided modes.

Guided modes are dispersive and travel with velocities which vary with frequency. The velocity of a guided mode depends on the material properties, thickness, and frequency. A dispersion curve, which describes their relationship, is fundamental to the guided wave analysis. The dispersion curve can be obtained by finding a solution to the homogeneous elastodynamic wave

equation (Rose, 2004b). This leads to a set of equations $\mathbf{M} \cdot \mathbf{N} = 0$, where $\mathbf{N}$ is the matrix of displacement vectors with unknown constants and $\mathbf{M}$ is the coefficient matrix of elastic constants, densities, thickness of the structure, wavenumber, and frequency. For a non-trivial solution to this system of equations, the determinant of the coefficient matrix should vanish, i.e., $|\mathbf{M}(\omega, k)| = 0$ where ω is the angular frequency and k is the wave number. The solution is a set of frequency-wave number $(f - k)$ pairs, dictating the trajectories for various modes.

In this thesis, we studied Lamb waves. Lamb waves, which are GWs traveling within a plate bounded above and below by air, have been well studied by many (Viktorov, 1967; Rose, 2004b). The dispersion characteristics are given by the following nonlinear equation

$$\frac{\tan(\beta d/2)}{\tan(\alpha d/2)} = \left[-\frac{4\alpha\beta k^2}{(k^2 - \beta^2)^2} \right]^{\pm 1} \tag{1.6}$$

where

$$\alpha^2 = \frac{\omega^2}{c_P^2} - k^2 \quad , \tag{1.7}$$

$$\beta^2 = \frac{\omega^2}{c_S^2} - k^2 \quad , \tag{1.8}$$

and d is plate thickness. The c_P and c_S are the longitudinal and transverse velocities

$$c_P = \sqrt{\frac{\lambda + 2\mu}{\rho}} \quad \text{and} \quad c_S = \sqrt{\frac{\mu}{\rho}} \tag{1.9}$$

where the density of bone is ρ, and the Lamé constants are λ and μ. Numerical techniques are used to find the solutions to Eq. (1.6).

Guided modes are classified as symmetric (S_n) or antisymmetric (A_n) depending on the particle motion through the plate. For a symmetric mode,

particle motion is symmetric across the thickness of the plate and the retrograde elliptical motion at the plate surface is parallel to the direction of energy propagation (Rose, 2004b; Cheeke, 2002). Antisymmetric mode exhibits particle motion that is antisymmetric along the plate thickness and the retrograde elliptical motion at the plate surface is perpendicular to the direction of energy propagation (Fig. 1.7). According to Eq. (1.6), the symmetric modes are acquired using the exponent '+1', while the anti-symmetric modes are attained using the exponent '−1'.

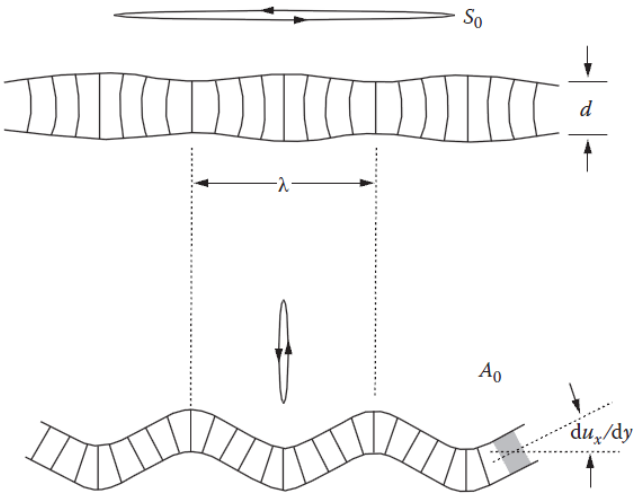

Figure 1.7: The deformation of particle planes and the retrograde elliptical motion at the plate surface of the A_0 and S_0 modes (Wenzel, 1992).

The application of GWs to study long bones is quite recent but the results so far are quite interesting. Nicholson et al. (2002) found the velocity of the fundamental Lamb mode A_0 differed by 15% between eight healthy and eight osteoporotic subjects (1615 m/s versus 1300 m/s). The same group studied a population of 106 pubertal girls and also found the velocity of a slow-traveling wave (1500 - 2300 m/s) consistent with that of the fundamental A_0 mode (Moilanen et al., 2003). Accordingly, Protopappas et al. (2006) identified four

low-order modes, S_0, S_1, S_2, and A_1 in an *ex vivo* study of an intact sheep tibia. Lee and Yoon (2012) found a strong correlation between the phase velocities of A_0 and S_0 modes with cortical thicknesses in bovine tibiae. Using a cylindrical bone model, Ta et al. (2006) found that the longitudinal mode, $L(0,2)$ was quite sensitive to the thickness change in the cortex. Tran et al. (2013b) examined the effect of soft tissue on guided waves using a bovine bone plate over a water half-space and overlaid by a 4-mm gelatin-based soft-tissue mimic. They found the presence of soft tissue increased mode density and number and the lowest-order mode (similar to the A_0 Lamb mode) was minimally affected by the addition of soft tissue. Kilappa et al. (2013) extracted the fundamental flexural GWs in 39 fresh human radii obtained from cadavers and found the group velocity was moderately correlated with the pQCT-based cortical width. Basically in most studies, the first few low-order guided modes have been consistently observed and further studied for their potential to characterize long bones.

1.5 Objectives of the Thesis

This study is motivated by the many advantages of the linear array system such as fast acquisition speed, small receptive element footprint, and its capability to steer the ultrasound beam. However, there are two issues relevant to the study. First, the active elements of the array probe communicate with one another when the probe is held in air and in no contact with any sample. The signals thus recorded are known as crosstalk signals. The crosstalk artifacts deteriorate the integrity of the ultrasound signals arising from real interfaces. Second, the use of beam steering to achieve preferential modal excitation is

limited and deserves a good investigation.

We use a linear array ultrasound system to study bone tissues. We have two hypotheses. We hypothesize that the crosstalk can be removed using an adaptive filter. Secondly, we hypothesize that by steering the beam, the guided modes can be preferentially excited.

1.6 Organization of the Thesis

The thesis is made up of four chapters.

Chapter 1 is an introductory chapter presenting the background literature and the objectives of the thesis.

Chapter 2 presents a study of exciting ultrasound using a phased array system with an array probe. In this chapter, we describe our Olympus ultrasonic phased array acquisition system, Tomoscan Focus LT$^{\mathrm{TM}}$. Then we describe an adaptive crosstalk cancellator algorithm to remove crosstalk artifacts in the data. Simulation data are used for verification. The algorithm is then applied to process experimental data with Plexiglas and bovine bone plates. The chapter is closed by concluding remarks.

Chapter 3 studies excitation of GWs using Tomoscan Focus LT^{TM} by beam steering with two array probes. The use of two arrays with one being the emitter and the other as a receiver eliminates the crosstalk artifacts. Beam steering allows GW modal selectivity by choosing optimized steering angle. The excitation function of a transducer is described. Steering the beam in a brass plate is used to verify the theory. Experimental data involving a bovine bone plate and different steering angles are provided. The chapter is closed by concluding remarks.

Chapter 4 summarizes the work presented in the thesis and concludes the thesis with some remarks on future directions.

Chapter 2

Excitation of Ultrasonic Waves Using A Phased Array System with A Single Array Probe

Communication among the elements within an ultrasound transducer array is known as acoustic crosstalk, or simply crosstalk. Fig. 2.1 illustrates the inter-element crosstalk generation. When an element is electrically excited with a reasonable voltage, the vibration of the element creates a pressure on neighboring elements and results in serial vibrations. This is due to cross-coupling between adjacent elements (Zhou et al., 2003). This acoustic crosstalk generates delayed output signals propagating in the transfer medium. Strong crosstalk is present in the forms of coherent signals such as direct wave, reflections, and guided waves traveling among the elements and the matching layer. When the transducer is held in contact with the material, the crosstalk signals appear as coherent noise and are detrimental as they interfere with the signals traveling within the sample (Kino and DeSilets, 1979; Baer and Kino, 1984), which might possibly lead to inaccurate interpretation of the data. Therefore, removing or filtering the crosstalk by means of signal processing is a necessary step prior to any further data analysis.

In this chapter, we examine the crosstalk of the probe and develop a signal processing method to eliminate crosstalk and recover the signals.

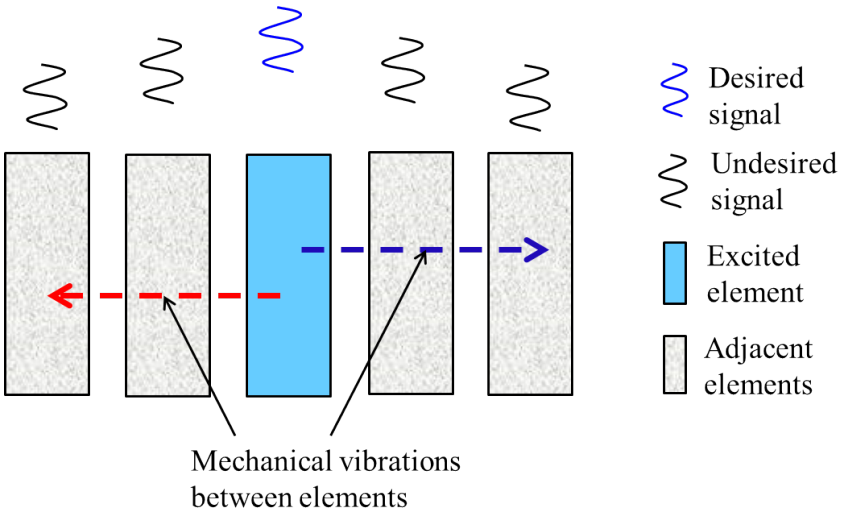

Figure 2.1: Possible crosstalk in an array probe.

2.1 Phased Array System

2.1.1 TomoScan FOCUS LT ™ Ultrasound Scanner

We used an Olympus TomoScan FOCUS LT™ Ultrasound PA system (Olympus NDT Inc., Canada) with an array probe in this study as shown in Fig. 2.2. The scanner was previously used to study scoliosis (Chen et al., 2012b). The system has the following specifications: 0.5 - 20 MHz bandwidth, 20 kHz pulsing rate, 10 - bit A/D converter, and up to 100 MHz sampling frequency. Real-time data compression and signal averaging are also available. The scanner has a high-speed data acquisition rate of 4 MB/s with maximum 1 GB file size and 8192 data points per A-scan (or time series). The unit is connected to a computer via an Ethernet port. The Windows XP-based computer was

loaded with Tomoview^{TM} software (Version 2.9 R6) to control the data acquisition process and modify the parameters of the ultrasound beam such as scanning mode, beam angle, focal position, and active aperture. The acquired data can be exported to the computer for further post-acquisition analysis using Matlab.

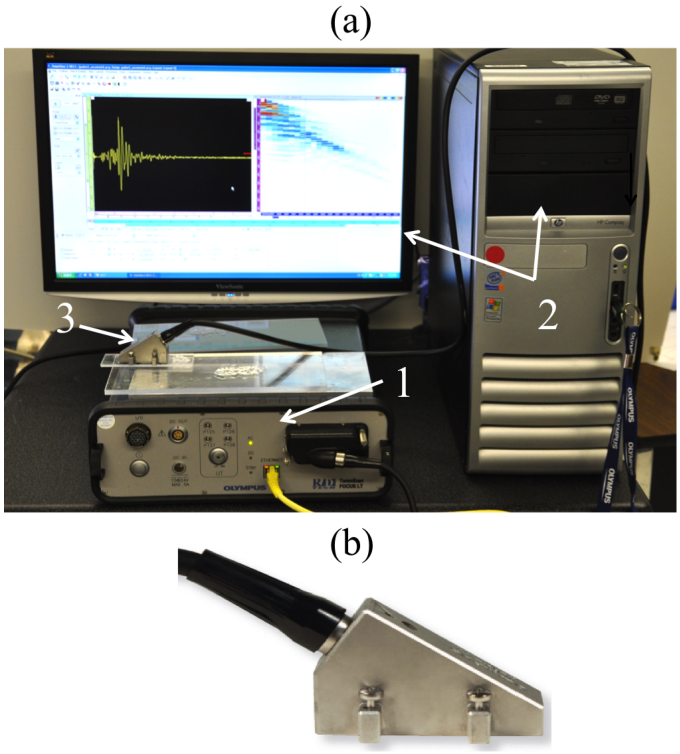

Figure 2.2: The ultrasound phased array system: (a) The TomoScan FOCUS LT^{TM} phased array acquisition system (1), the Windows XP-based computer with the TomoView^{TM} software to control the acquisition process (2), and the probe unit (3). (b) the 64-element phased array probe.

One of the important features of the scanner is that it is able to support multi-probe operations such as a single-transducer-multi-element probe combination or two multi-element probes up to 128 elements. Beam steering and focusing (transmit focus) at oblique angles can be achieved by electronically delaying the firing of the elements without mechanical movement. Receive-

focusing is also possible. The returning echoes are stored, delayed, and then summed to produce an ultrasound signal. Dynamic focusing is available to extend the lateral resolution over a depth range. The ultrasound transducer used is a 2.25-MHz 64-element array probe (2.25L64). The probe has an active area of 48 mm (length) by 12 mm (elevation) with a pitch of 0.75 mm (Fig. 2.3a). Pitch is defined as the distance between the centers of two adjacent elements. A rexolite matching layer covers the array to reduce the acoustic impedance difference between the piezoelectric ceramic and scanned objects. Fig. 2.3b illustrates further the principle of beam steering. Pulsing individual elements or groups of elements with different delays creates a series of traveling wavefronts with delay in onset times. These wavefronts meet, interfere, and combine in a complicated way. Destructive and constructive interference occurs. When they are in phase, the wave energies reinforce. When they are out of phase, the wave energies cancel each other. Constructive interference takes place at certain phrases, beyond which destructive cancellation occurs, and therefore beam steering is accomplished.

2.1.2 Data Acquisition

For the Plexiglas plate experiment, we chose to use a single element as the emitter and receiver. The first element was electrically excited with a 40-V pulse while the other 63 elements operated as receivers. The crosstalk signals inside the transducer were recorded and measured by operating the probe in air without contact with any object. We considered two thicknesses of Plexiglas, 9 and 24 mm, with a compressional wave speed of 2700 m/s and a shear wave speed of 1370 m/s. The plate rested on two rubber corks (Fig. 2.4), the probe was in contact with the plate, and the two steel bars applied appropriate

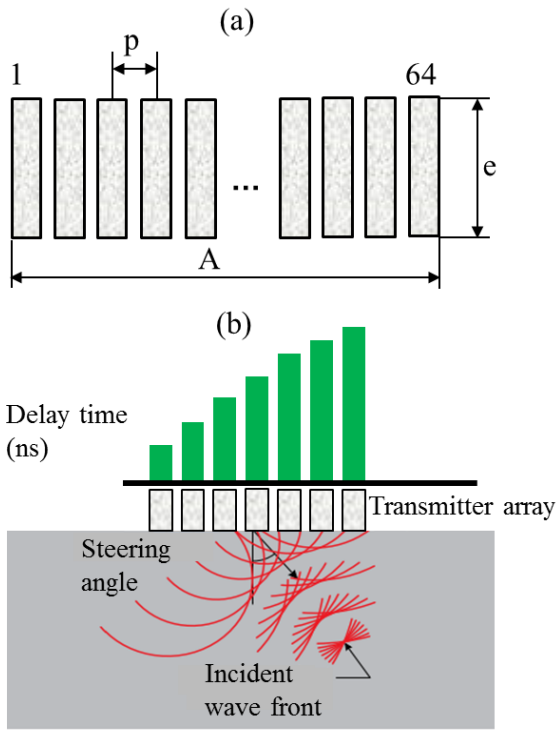

Figure 2.3: (a) The dimensional parameters of an array transducer: $p-$the pitch, $e-$the elevation, and $A-$the aperture. (b) An illustration of the principle of beam steering by delaying the firings of the elements successively (modified from Olympus NDT (2007)).

pressure on the probe against the plate to ensure good contact. Ultrasound gel was used between contacts to ensure good coupling in all experiments. Each A-scan, which was summed 16 times and averaged, was 2000-points long with a sampling interval of 0.02 μs. The data had 63 A-scans of 0.75 mm spacing. The offset spanned from 0.75 mm to 47.25 mm with an aperture of 46.5 mm. Before analysis, data were self-normalized and filtered with a trapezoidal (0.1/0.2/2.9/3.0 MHz) bandpass filter .

For the bone plate experiment, we chose a group of 3 elements as the emitter and receiver to increase input power. A desk-mounted vice grip was used to hold the plate firmly (Fig. 2.5). The probe was then placed on the sample

with the steel bars pressing against the probe, similar to the Plexiglas experiment. Other procedures followed the Plexiglas experiment. The data had 59 A-scans spaced by 2.25 mm. The offset spanned from 2.25 mm to 44.25 mm with an aperture of 42 mm. We applied a trapezoidal (0.1/0.15/1.9/2.0MHz) bandpass filter to the data prior to further analysis.

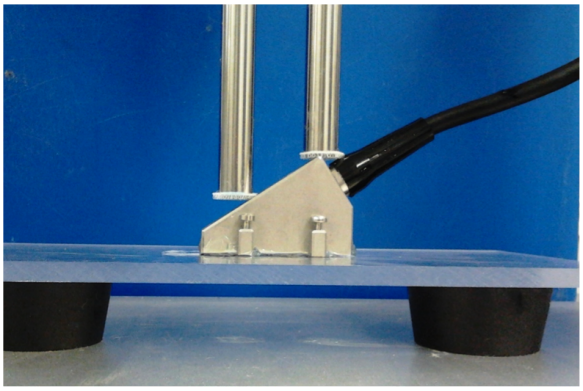

Figure 2.4: The phantom experiment with the 64-element array probe on a 9-mm thick Plexiglas plate.

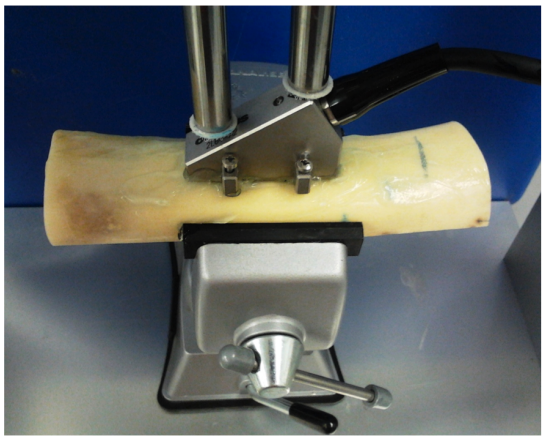

Figure 2.5: The *in vitro* experiment with the 64-element array probe on a 6-mm thick bovine bone plate.

2.1.3 Resolution Measures

2.1.3.1 Near Field Length

The calculated near field length, L is

$$L = \frac{kA^2 f}{4v} \tag{2.1}$$

where the aspect ratio constant k, which is the ratio between the short and long dimensions of the transmitter, is 0.99; A, the transmitter aperture; f, the frequency; v, the sound velocity of the coupling medium. Since f is 2.25 MHz and v is 1500 m/s, L is 0.21 mm for a single source ($A = 0.75$ mm) and 1.89 mm for a 3-element group ($A = 2.25$ mm).

2.1.3.2 Axial Resolution

Axial resolution, Δz is the minimum distance along the beam axis for which two adjacent defects located at different depths are clearly displayed as shown in Fig. 2.6 (Olympus NDT (2007)),

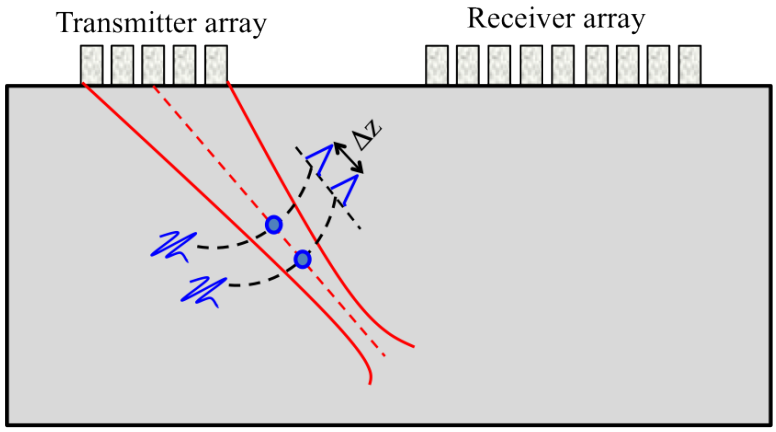

Figure 2.6: A schematic diagram of axial resolution of the beam (modified from Olympus NDT (2007)).

$$\Delta z = \frac{\text{pulse length}}{2}. \tag{2.2}$$

The pulse length can be calculated by the number of cycles $\times$ wavelength of the pulse (Bushberg and Boone, 2011). A good axial resolution is possible by shortening pulse duration (high-damped probe and/or higher frequency).

2.1.3.3 Lateral Resolution

We also require good lateral resolution parallel to the aperture. Lateral resolution, Δy is the minimum distance between two adjacent defects located at the same depth Olympus NDT (2007),

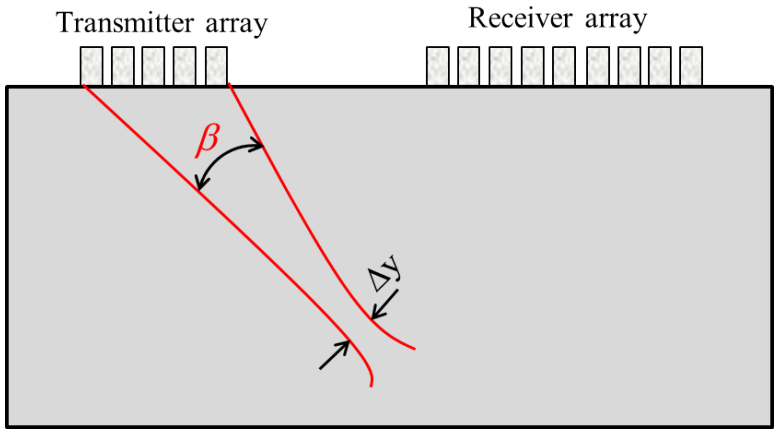

Figure 2.7: A schematic diagram of lateral resolution of the beam (modified from Olympus NDT (2007)).

$$\Delta y \simeq \frac{0.11 v_{\text{sample}}}{f \sin(\beta/2)} \tag{2.3}$$

where v_{sample} is ultrasonic velocity of the sample, f is the frequency, and β is the effective aperture angle, beneath which the virtual probe aperture (aperture of the element group) is seen from the focal point (Appendix A).

2.2 The Linear $\tau - p$ Transform

The discrete Radon transform (RT), also known as the τ-p transform, is defined by summing the amplitudes along a line $t = \tau + px$ with moveout px (Fig. 2.8) where p is the ray parameter (or slowness) and τ is the the arrival time at zero-offset (zero-offset time intercept) Gu and Sacchi (2009). Consider a series of ultrasonic time signals $d(t, x_n)$ acquired at different offsets, x_0, x_1, ..., x_{N-1} where t denotes time and the x-axis is not necessarily evenly sampled. We write the time signals, d, as a superposition of Radon signals, $m(\tau, p)$:

$$d(t, x_n) = \sum_{k=0}^{K-1} m(\tau = t - p_k x_n, p_k), \quad n = 0, ..., N-1. \tag{2.4}$$

where p is sampled at p_0, p_1, ..., p_{K-1}. Taking the temporal Fourier transform (FT) of Eq. (2.4) yields

$$\hat{D}(f, x_n) = \sum_{k=0}^{K-1} M(f, p_k) e^{-i2\pi f p_k x_n}. \tag{2.5}$$

where f is the frequency. Rewriting Eq. (2.5) using matrix notation for each frequency gives

$$\hat{\mathbf{D}} = \mathbf{L}\mathbf{M} \tag{2.6}$$

and

$$\mathbf{L} = \begin{bmatrix} e^{-i2\pi f p_0 x_0} & \dots & e^{-i2\pi f p_{K-1} x_0} \\ \vdots & \ddots & \vdots \\ e^{-i2\pi f p_0 x_{N-1}} & \dots & e^{-i2\pi f p_{K-1} x_{N-1}} \end{bmatrix}. \tag{2.7}$$

A low-resolution adjoint RT can be calculated using the following equation

$$\mathbf{M}_{\text{Adj}} = \mathbf{L}^H \hat{\mathbf{D}} \tag{2.8}$$

where $\mathbf{L}^H$ is the adjoint or complex-conjugate transpose operator. The adjoint operator is a matrix transpose and is not the inverse operator. The transformation by $\mathbf{L}^H$ is not unitary, that is, $\mathbf{L}\mathbf{L}^H \neq \mathbf{I}$. However, the adjoint sometimes

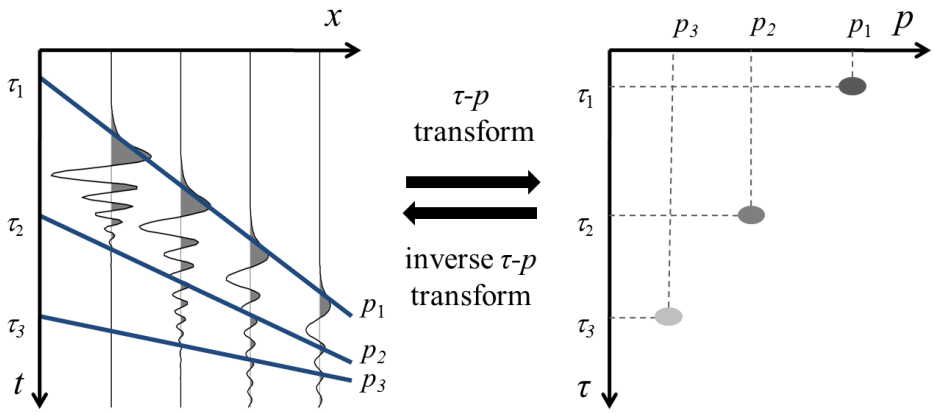

Figure 2.8: The schematic diagram for forward and inverse linear τ-p transform. The records are summed along straight lines with different slopes, p and time intercepts, τ. Stacking along p_1 goes through strong peaks of the records and thus yields a strong amplitude focus in the τ-p panel (dark gray ellipse) while stacking along p_2 encounters amplitudes of opposite polarities and thus leads to less Radon energy. Stacking along p_3 leads to trivial Radon energy due to very small amplitudes of the signals (modified from Gu and Sacchi (2009)).

outperforms the inverse operator in the presence of noise and incomplete data information (Claerbout, 2004).

To enhance the imaging resolution of the dispersive energies, we can cast the problem as an inverse problem by seeking a least-squares solution to Eq. (2.6) with a Cauchy regularization (Sacchi, 1997). We seek a Radon solution or model, $\mathbf{M}$, which minimizes the following l_2-norm cost function in a least-square sense

$$J = \|\mathbf{LM} - \hat{\mathbf{D}}\|^2 + \mu \sum_{k=0}^{K-1} ln(1 + M_k^2/\sigma^2). \tag{2.9}$$

The first term is the misfit term, which measures how well the model predicts the data and the second term is the regularization term. The regularization refers to the constraint imposed explicitly on the estimated model during inversion. The purposes of the regularization term are to improve focusing power of the solution and also to stabilize the solution. The degree of contribution

of the regularization term depends on the value of the trade-off parameter or hyper-parameter, μ. By taking the derivatives of J with respect to the model $\mathbf{M}$ and equating to zero, we arrive at the high resolution Radon solution

$$\mathbf{M}_{\mathrm{MR}} = (\mathbf{L}^H\mathbf{L} + \mu\mathbf{Q}(\mathbf{M}))^{-1}\mathbf{L}^H\hat{\mathbf{D}} \tag{2.10}$$

where $Q_{ii} = \frac{1}{(1+M_i^2/\sigma^2)}$ is a diagonal weighting matrix and σ^2 is the scale factor of the Cauchy distribution.

Eq. (2.10) is a non-linear system of equations, which can be solved by the iterative re-weighted least-squares scheme for each frequency (Scales et al., 1988). In our work, we used $\sigma = 0.8$. The choice of the μ-value was based on the L-curve to balance between the predicted error and the regularization term and usually the values around the local minimum point, also known as the knee or corner point, are used (Engl and Grever, 1994; Hansen, 1992). We also found that 4 iterations were sufficient to produce good results. Once $\mathbf{M}$ is determined for all frequencies, we perform an inverse FT to map $\mathbf{M}(f, p)$ back to the time domain $\mathbf{m}(\tau, p)$, creating a $\tau - p$ Radon panel. In the τ-p domain, windowing can be used to extract wavefields of desired slownesses while muting the others. Finally, the dispersion curve or $f - c$ panel is obtained by replacing $p = 1/c$ in $\mathbf{M}$ via linear interpolation. We reconstruct the filtered t-x signals by performing the operations in the following order: Fourier-transform the $\tau - p$ panel to the f-p panel, map the f-p panel to the f-x panel via Eq. (2.6) using the Radon operator $\mathbf{L}$, and inverse Fourier-transform the f-x panel to the t-x domain.

To avoid aliasing, sampling frequency should be greater than twice the maximum frequency. Also sampling in slowness, Δp, must be smaller than $1/(r_{aper} f_{max})$ where r_{aper} is the aperture and f_{max} is the maximum frequency

of the data (Turner, 1990).

2.3 Adaptive Crosstalk Cancellator

Recent work suggests the use of adaptive noise cancellator (ANC) as an alternative crosstalk removal method. Th ANC is a digital filter that predicts the noise and subtracts it from the data to obtain the desired noise-free signals. The prediction is adaptive by self-adjusting its transfer function by minimizing the error signal. This technique has been successfully applied in many engineering and biomedical fields. For example, Li and Hayward (2011) exploited an ANC to recover the true velocity signal from Doppler ultrasound. Brady et al. (2012) enhanced identification of material defects by using an ANC to eliminate backscattered noise arising from internal micro-structures. Dalgaard et al. (2012) applied an ANC to filter powerline harmonics from the magnetic resonance sounding signals in a ground water survey. Wirnitzer et al. (1998) aimed to cancel interference among ultrasonic sensor arrays by using an ANC for tracking and localization.

2.3.1 Adaptive Crosstalk Cancellator

An adaptive noise cancellator (Fig. 2.9) assumes that the recorded data contains signal and noise, which is uncorrelated with the signal and an independent measured reference noise is available. The cancellator predicts the noise from the reference and subtracts it from the data to output the predicted noise-free signals, which is the error signal. The error signal is fed back into the filter to adjust adaptively the filter coefficients to provide a better estimate of the signal in a least-squares-sense (Widrow et al., 1975). In our study, the noise is the crosstalk and thus, we call the adaptive filter the adaptive crosstalk

cancellator (ACC).

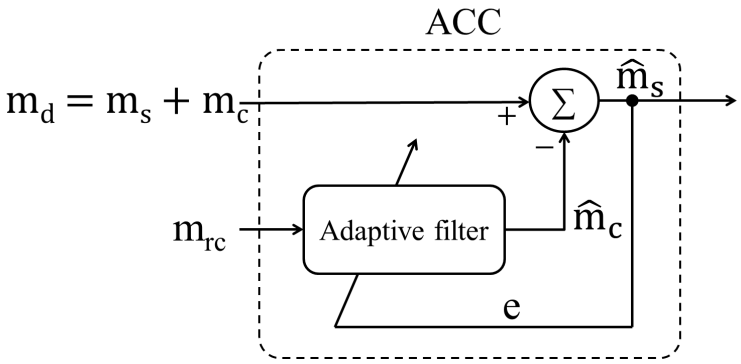

Figure 2.9: Principle of adaptive crosstalk cancellator(Widrow et al., 1975).

Let $\mathbf{m}_d$ and $\mathbf{m}_{rc}$ be the $\tau - p$ representation of the recorded data and reference crosstalk. The high resolution RT was used in this chapter. The reference crosstalk can be acquired with the transducer held in air (without contacting any material). The data, $\mathbf{m}_d$ contains the desired signal, $\mathbf{m}_s$ and the crosstalk, $\mathbf{m}_c$. The ACC uses the reference crosstalk to estimate the predicted crosstalk, $\widehat{\mathbf{m}}_c$ by means of the filter, $\mathbf{w}$,

$$\begin{aligned}\widehat{m}_c(i) = m_{rc}(i)w_0^{i-1} + m_{rc}(i-1)w_1^{i-1} + \ldots \\ + m_{rc}(i - L_w + 1)w_{L_w-1}^{i-1}\end{aligned} \tag{2.11}$$

where i is the time index and L_w is the filter length. We write $\mathbf{w}^i$ to denote an updated estimate of $\mathbf{w}$ at iteration i. The error, $\widehat{m}_s(i) = m_d(i) - \widehat{m}_c(i)$, is then used in a feedback loop to adaptively update the filter coefficients at next iteration. We adopted the normalized least-mean-squares algorithm to adjust the filter coefficients (Sayed, 2003)

$$\mathbf{w}^i = \mathbf{w}^{i-1} + \frac{\beta}{\alpha + \|\mathbf{m}_{rc}^i\|^2}(\mathbf{m}_{rc}^i)^*[m_d(i) - \widehat{m}_c(i)] \tag{2.12}$$

with the initial condition

$$\mathbf{w}^{-1} = \{0, 0, \ldots, 0\} \tag{2.13}$$

where $\mathbf{m}_{rc}^{i} = [m_{rc}(i), m_{rc}(i-1), \ldots, m_{rc}(i-L_w+1)]$, the asterisk denotes the transpose conjugate, and β is the step-size. In this work, we used a 4-tap filter, i.e., $L_w = 4$. The α is a small non-zero constant, which took the value of 10^{-4}, and was used to stabilize the solution when $\|\mathbf{m}_{rc}^{i}\| \approx 0$. For a convergent condition, $0 \leq \beta \leq 2$ (Haykin, 1996) and we chose $\beta = 0.1$ based on the smallest MSE (mean-squares-error).

2.3.2 Validation of Adaptive Crosstalk Cancellator

To validate the ACC algorithm, we simulated a data set with four linear and hyperbolic events. The travel times of the linear and hyperbolic arrivals were calculated by $t = pv + \tau_0$ and $t = \sqrt{x^2 + 4h^2}/v + \tau_0$ respectively where x is the offset, h is the thickness of the layer, p is the slowness, v is the material velocity of the layer, and τ_0 denotes the delay time. For each offset, a time series was simulated with impulses at arrival times of the events. The time series was then convolved with a Berlage wavelet (Le, 1998):

$$f(t) = Bt^m \mathrm{e}^{-bt} \cos(\omega_0 t + \varphi_0) H(t) \tag{2.14}$$

and $H(t)$ is the Heaviside function

$$H(t) = \begin{cases} 0 & \text{for } t < 0 \\ 1 & \text{for } t \geqslant 0 \end{cases} \tag{2.15}$$

where $m = 4$, $b = 7$ rad/μs, $f_0 = 1.25$ MHz, and $\varphi_0 = \pi/2$. The constant B took the value of 2 for signals and reference crosstalk.

Forty time series up to 15 μs were simulated with offset spanning from 0.75 mm to 30 mm. The reference crosstalk was made up of one linear event and a

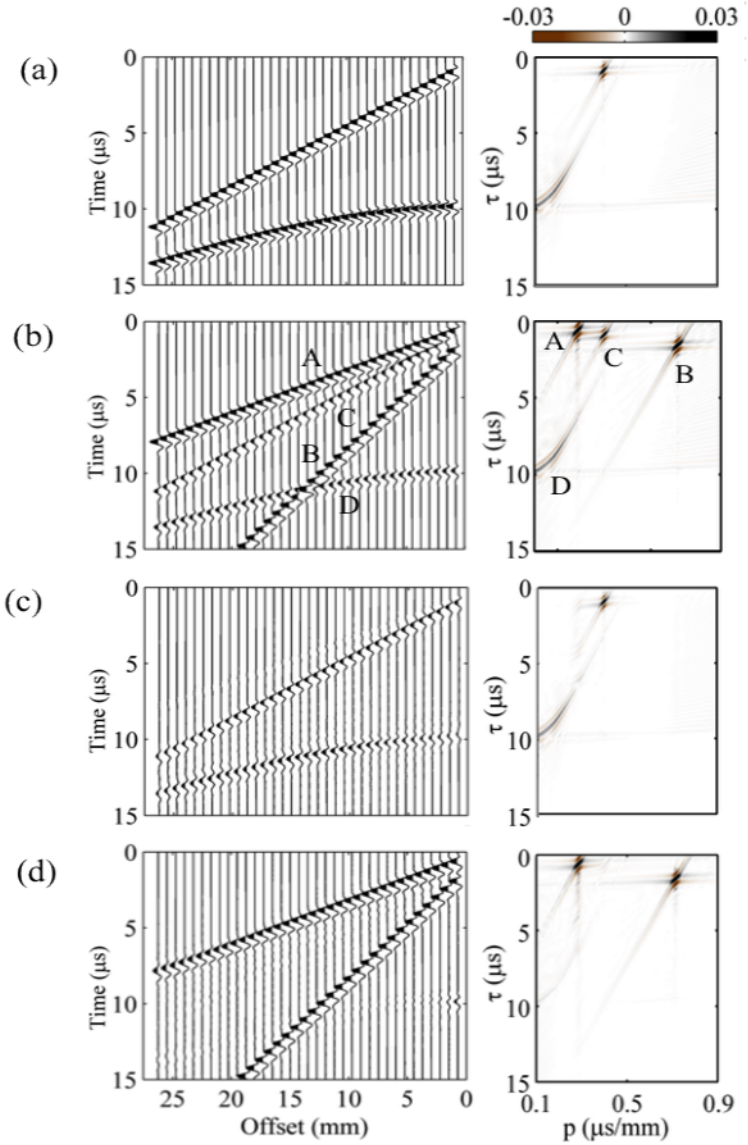

Figure 2.10: A noiseless example shows the simulated and ACC-filtered crosstalk and signals with their corresponding $\tau - p$ panels. (a) The simulated reference crosstalk; (b) The simulated data consisting of signals (A and B) and crosstalk (C and D) where the amplitudes of the latter are only half of those of the reference crosstalk; (c) The predicted crosstalk; (d) The ACC-filtered signals.

multiple reflection (Fig. 2.10(a)). The linear event had a delay of 0.9 μs and slowness of 0.4 μs/mm (2500 m/s). The 10-μs delayed reflection was made up of three multiple reflections with very small delays, each of which traveled at slowness of 0.5 μs/mm (2 km/s) in a 3-mm thick layer. Being delayed by 0.6 sec and 1.6 sec, the signals, A and B, traveled at slowness of 0.286 μs/mm (3.5 km/s) and 0.769 μs/mm (1.3 m/s) respectively as shown in Fig. 2.10(b). The reference crosstalk was also used as crosstalk events (C and D in Fig. 2.10(b)) but their amplitudes were halved in comparison with the reference.

The ACC-predicted crosstalk is shown in Fig. 2.10(c) while the ACC-filtered signals are shown in Fig. 2.10(d). The filter was not able to remove all crosstalk events and there is some residual crosstalk around 10 μs for the first few close-offset records (Fig. 2.10(d)). However, their amplitudes are very small. We compared the predicted arrivals with their simulated counterparts at 17.25-mm offset. The filtered signals track well with the simulated signals with a relative MSE of 13% and 9% for the mismatch of the first and second peaks respectively (Fig. 2.11).

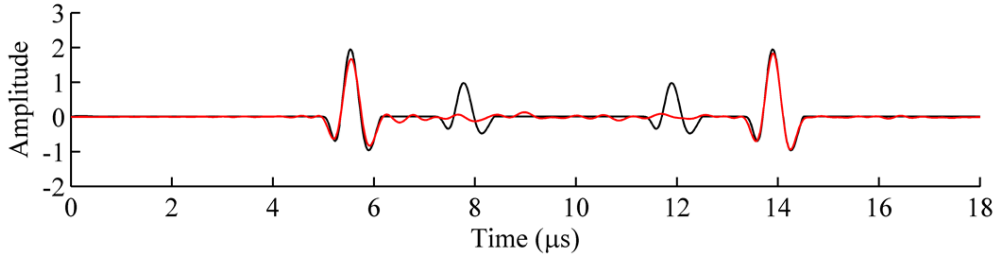

Figure 2.11: Comparison between the ACC-filtered (red) and simulated (black) data at 17.25 mm offset.

We also investigated the MSE between the signal and filtered signal as a function of the step-size β and filter length, L. Fig. 2.12 shows that the MSE

is at a minimum when $L = 4$ and β=0.1.

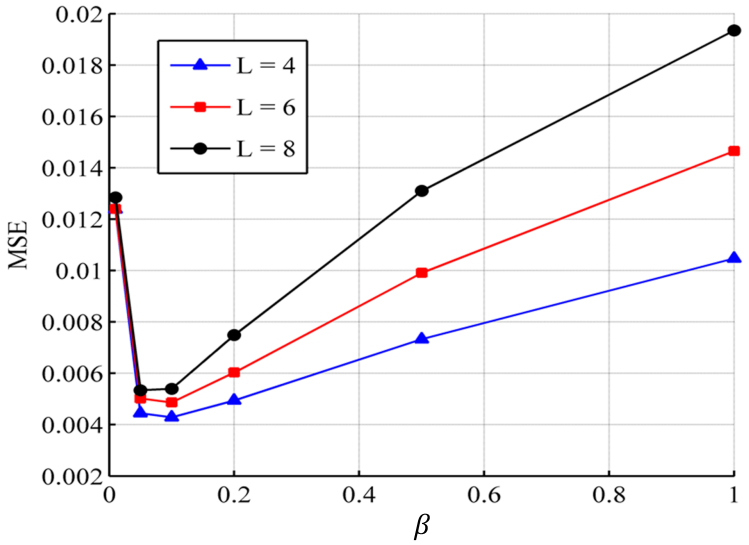

Figure 2.12: The MSE between the signal and filtered signal for different values of step-size β and filter length L.

A noisy data set was also simulated by adding Gaussian noise to the previous noiseless data (Fig. 2.13). The SNR (signal-to-noise ratio) was 10 dB. Both the $t - x$ and $\tau - p$ panels show the background noise. However the signals and their corresponding Radon energy clusters are clearly seen. Similar to the noiseless case, we compared the predicted arrivals with their simulated counterparts at 17.25-mm offset. The filtered signals (Fig. 2.14) shows that the crosstalk has been removed. As well, the random noise has also been filtered in the process. This is possible because the $\tau - p$ transform sums the amplitudes of the waveforms, thus reinforcing coherent signals and eliminating randomness.

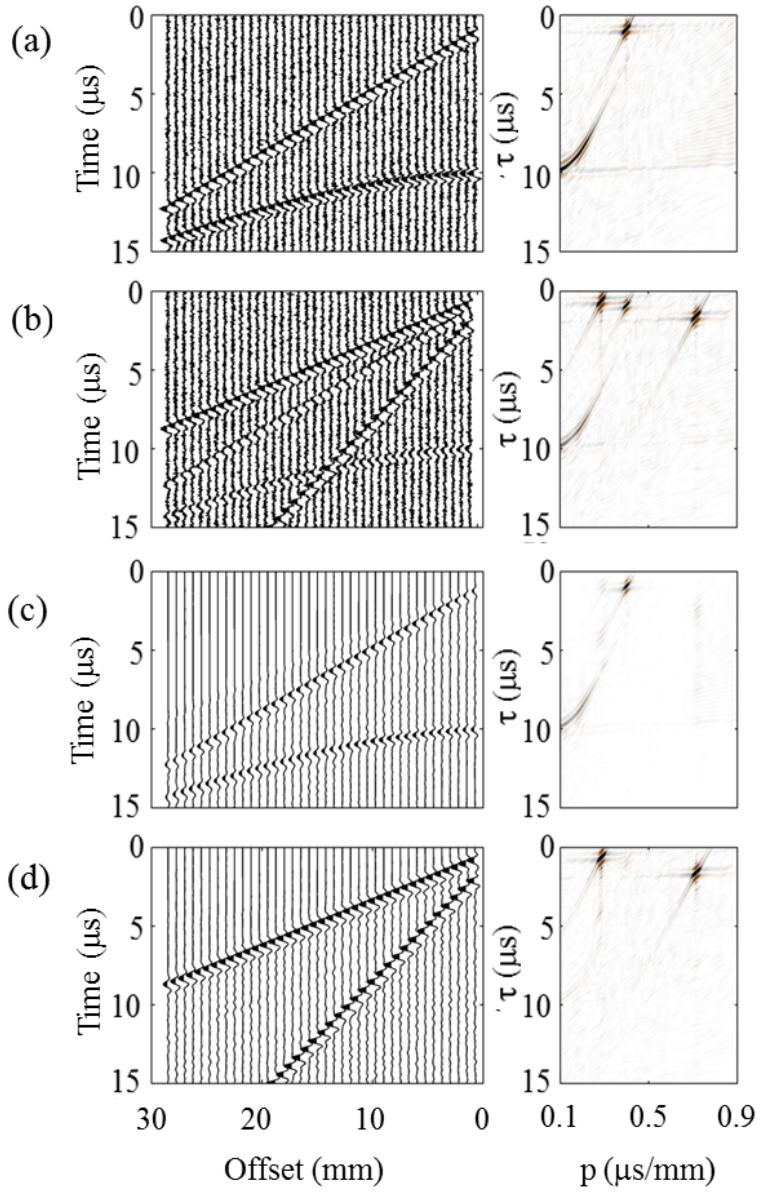

Figure 2.13: A noisy example shows the simulated and ACC-filtered crosstalk and signals with their corresponding $\tau - p$ panels. The SNR is 10 dB. (a) The simulated reference crosstalk; (b) The simulated data consisting of signals (A and B) and crosstalk (C and D) where the amplitudes of the latter are only half of those of the reference crosstalk; (c) The predicted crosstalk; (d) The ACC-filtered signals.

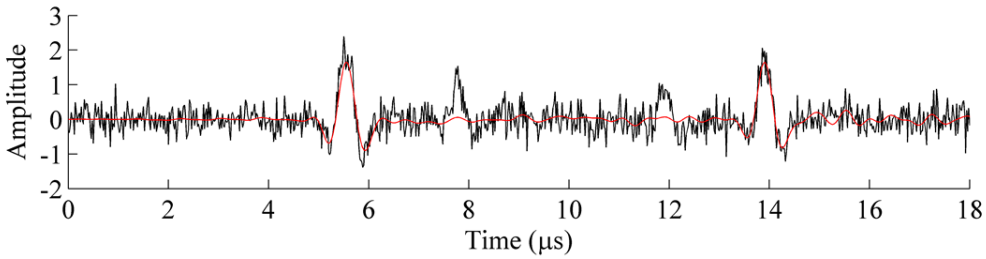

Figure 2.14: Comparison between the ACC-filtered (red) and noisy (black) data at 17.25 mm offset.

2.4 Applications

2.4.1 24-mm Thick Plexiglas plate

Fig. 2.15 shows the reference crosstalk in three domains: $(t-x)$, $(\tau-p)$, and $(f-c)$. The records were self-normalized, that is, each record was normalized by its own absolute maximum. The reference crosstalk was recorded with the array being held in air and in no contact with any material. Three main types of arrivals can be clearly identified with different phase velocities and traveling times. They are the small-amplitude, high-frequency linear event (A) traveling with a phase velocity around 3.8 km/s, a low-frequency linear dispersive wave train (B) traveling at a range of velocities 1.6 - 2.5 km/s, and the later arrivals (C), which are the hyperbolic reflection events traveling at 3.2 - 5 km/s. They correspond respectively to the direct wave (1), perhaps guided waves propagating in the matching layer (3), and reflections among elements (2) within the array probe as shown in Fig. 2.16. This crosstalk is not desirable as it interferes with the real information-carrying signals traveling through the target material. The crosstalk signals can also be distinguished in a $\tau-p$ plot (Fig. 2.15(b)). When the offset is small, both type A and B arrivals have close-to-zero τ-values, The type A event has a very close-to-

zero time-intercept and is linear with a constant 0.26 μs/mm slowness (phase velocity of 3.8 km/s). The Type B arrivals also have small τ-values but are different from the type A event in their dispersive characteristics. Instead of having a constant slowness, the wave train travels with a range of slownesses 0.4 - 0.625 μs/mm, which is well separated from the slowness of the type A arrival. The type C arrivals are reflection events with large τ-values between 7 and 10 μs and a slownesses $0.2 - 0.35$ μs/mm (phase velocity of 2.8 - 5 km/s). The dispersion panel (Fig. 2.15(c)) shows two strong dispersive modes. The high-speed modes (3.5 - 5 km/s) are the strong reflection (C) and the weak direct (A) arrivals while the slow-traveling modes are the guided wave energies (B).

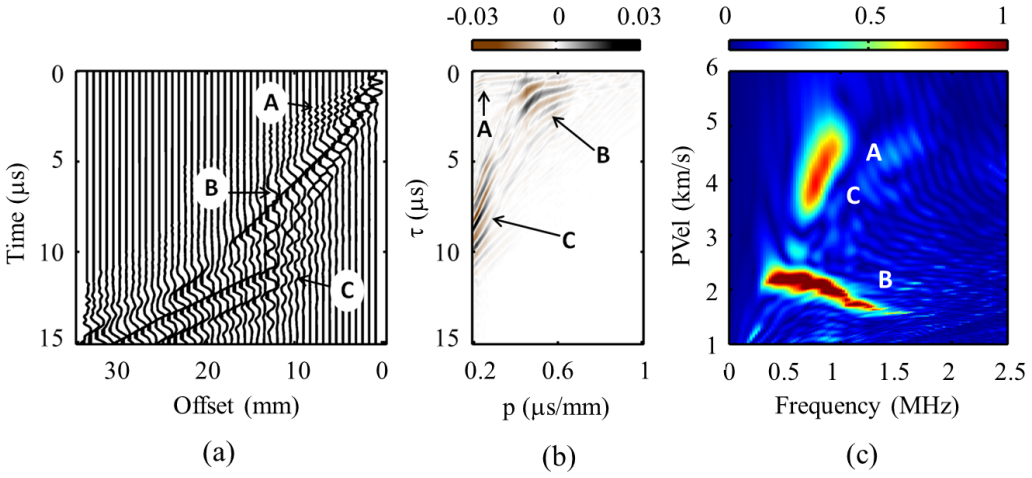

Figure 2.15: The reference crosstalk plotted in three different domains: (a) $(t-x)$, (b) $(\tau-p)$, and (c) $(f-c)$. The letters A, B, and C denote the three different arrivals existing in the transducer array, which correspond to the direct wave, guided waves propagating in the matching layer, and reflection arrivals (refer to Fig. 2.16 for further details).

The recorded data (Fig. 2.17) shows a mixture of crosstalk and real signals propagating in the 24-mm Plexiglas plate. Except for the guide wave energies

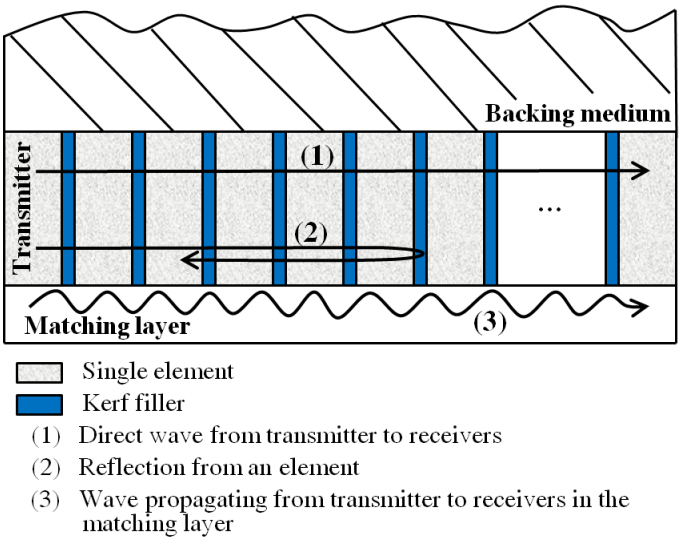

Figure 2.16: Crosstalk inside an array transducer.

(B), the other Radon crosstalk energies (A and C) are weak. Two different Radon signal clusters appear around the same intercept time (0 - 2 μs) but with different slownesses, approximately 0.37 and 0.75 μs/mm (see Fig. 2.17(b)). The signal cluster E at 0.37 μs/mm interferes with the crosstalk cluster B while the other signal cluster F is well separated from the rest. These two modes travel at around 2.8 and 1.4 km/s and are easily identified from crosstalk modes in the $(f-c)$ domain (see Fig. 2.17(c)). These modes are not dispersive as the phase velocities are quite constant for an extended range of frequencies (over 0.8 MHz for E and from 0.8 to 1.7 MHz for F). They quite likely correspond to the P-wave, S-wave, and Rayleigh waves traveling within the Plexiglas with velocities being 2.73, 1.43, and 1.33 km/s, respectively. The S-wave, and Rayleigh waves come close together. The energies bounded between these two modes are the slow-traveling crosstalk energy (B) as seen in Fig. 2.15(c) and deemed to be removed by the ACC filter.

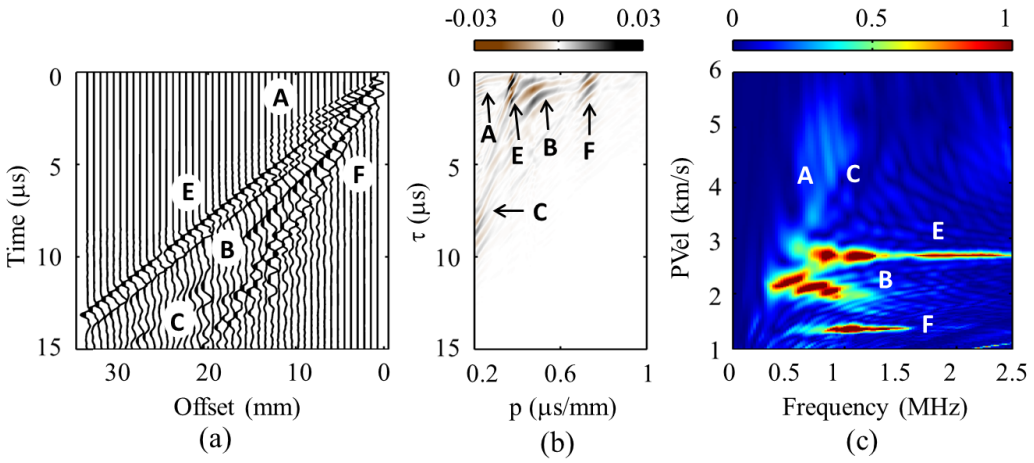

Figure 2.17: The crosstalk-corrupted data for the 24-mm thick Plexiglas plotted in three different domains: (a) $(t-x)$; (b) $(\tau-p)$ and (c) $(f-c)$.

We compared three crosstalk-filtering methods to remove the crosstalk energies in Fig. 2.18. The first method is the conventional ACC implemented in the $t-x$ domain, that is, the recorded data and reference crosstalk were in the $t-x$ space. Fig. 2.18a shows the presence of some residual crosstalk energy (B); otherwise, most of the crosstalk energies have been removed. However the mode (F) was also effected and the modal energy was greatly reduced. Only mode E was recovered with high degree of certainty. For the second method, we transformed the data to the $\tau-p$ space and subtracted the reference crosstalk from the data. The filtered signals are inferior (Fig. 2.18b). All crosstalk energies, mainly B and C, were not totally removed. This was because the amplitudes of the data and reference crosstalk were not the same and as such subtraction did not cancel the crosstalk totally. Also, the filtering was not adaptive. Lastly, we applied the ACC to the data in the $\tau-p$ space. The results (Fig. 2.18c) are the best among the three methods. The crosstalk energies were successfully removed and both modes, E and F, were recovered

faithfully with high degree of coherency and continuity.

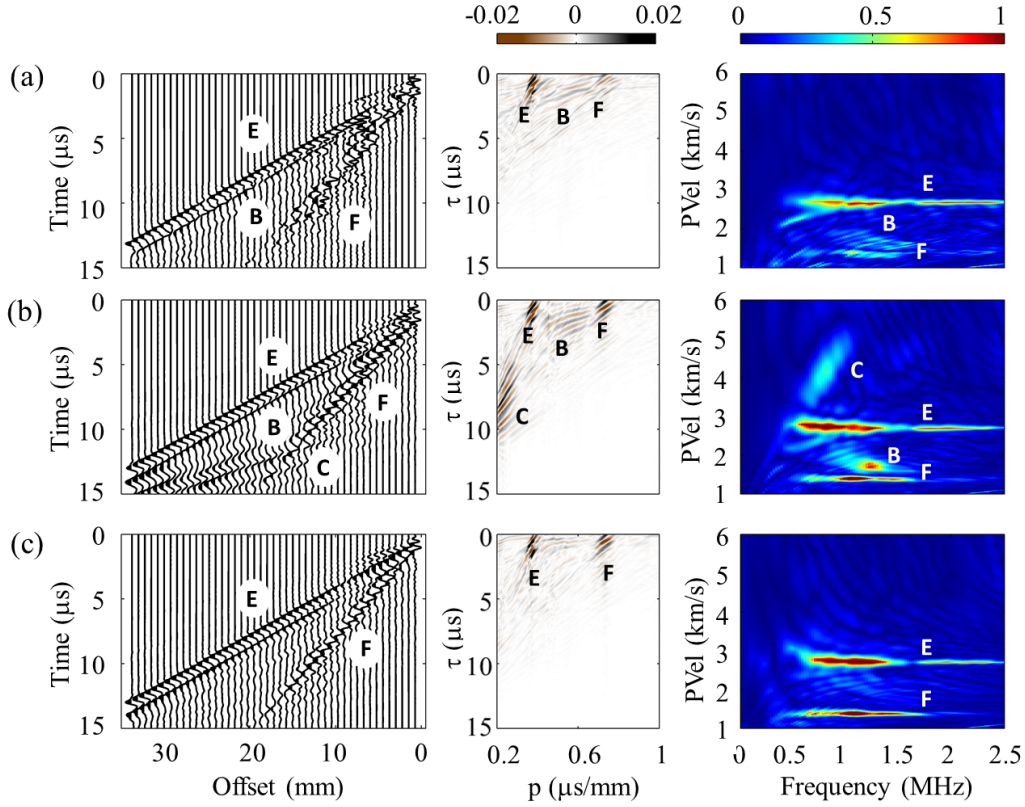

Figure 2.18: The crosstalk-filtered signals for the 24-mm thick Plexiglas using three approaches: (a) the conventional ACC in $(t-x)$, (b) normal subtraction in $(\tau-p)$, and (c) ACC in $(\tau-p)$. The results are represented in three different panels ($(t-x)$, $(\tau-p)$, and $(f-c)$) for verification.

2.4.2 9-mm Thick Plexiglas plate

We considered further a thinner 9-mm Plexiglas case to facilitate multiple reflections. The thickness-to-wavelength ratio was 7.5 and therefore bulk waves dominated. The acquired data shows strong multiple reflections in Fig. 2.19a, which overlap and overshadow the primary signals and crosstalk. Since the reference multiple reflections are not available, adaptive subtraction algorithms can not remove them. However, these multiples come at later times than the

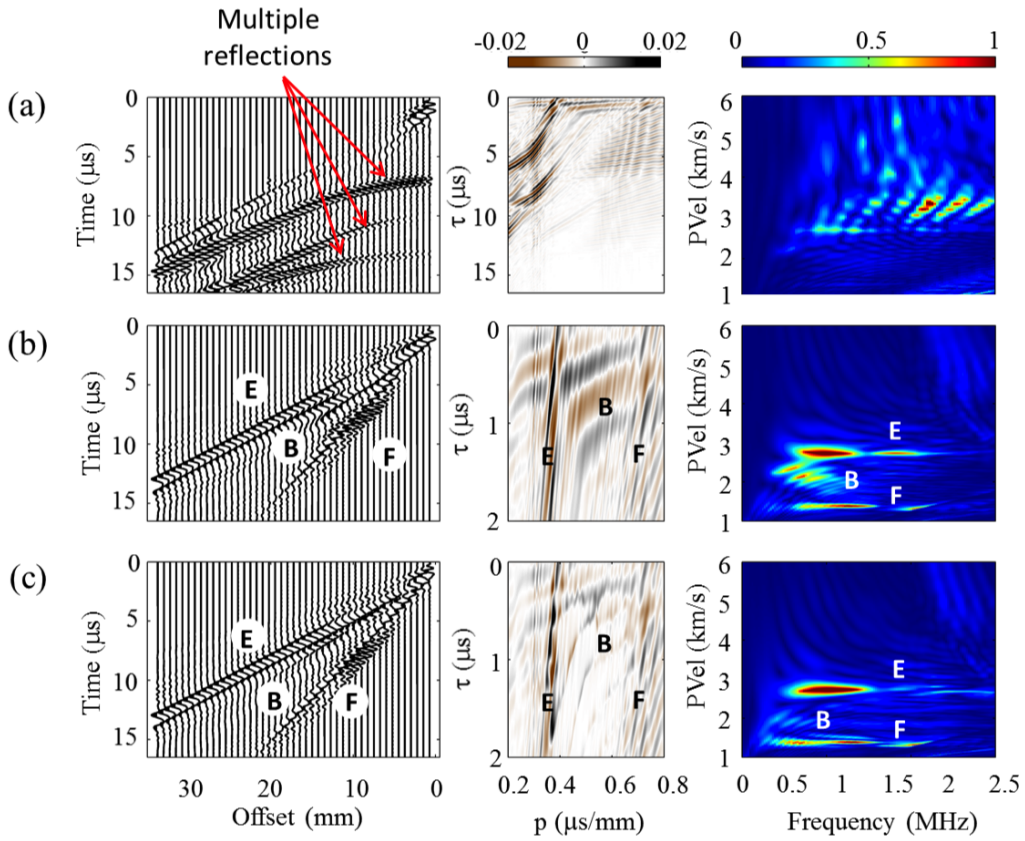

Figure 2.19: Crosstalk removal in a 9-mm thick Plexiglas: (a) the original data, (b) the data after multiple reflections are muted in the $\tau - p$ domain, and (c) the ACC-filtered signal.

other arrivals, as shown in the $\tau - p$ panel. To avoid the inclusion of these multiples, we only considered the first 2.0 μs of the data. We muted all Radon energies longer than 2.0 μs in the Radon panel and inverted the $\tau - p$ signals back to the $t - x$ domain. Fig. 2.19b shows the data after muting. Two strong signals (E and F) and the crosstalk (B) can be identified. Fig. 2.19c shows the data after ACC filtering. The filter removed significantly most of the crosstalk energy (B) but failed to remove it totally as shown in the $t - x$ and $\tau - p$ panels. However the crosstalk energy is small and does not show in the $f - c$

panel and the two modes (E) and (F) are sharply imaged with high resolution.

2.4.3 6-mm Thick Bovine Bone Plate

The bone plate was thick is compared to the wavelength with a thickness-to-wavelength ratio of 5. Since the offset was also small, the data is rich with bulk waves, notably P- and S-waves. The former traveled at a velocity of 3.9 km/s while the latter at 1.8 km/s. Similar to the 9-mm Plexiglas case, the bone data shows multiple arrivals. Following the previous example, we muted in the Radon panel all energies after 2 μs. The data, after the exclusion of the multiple reflection energy, shows three distinct arrivals (Fig. 2.20(b)): E and F corresponding to the P- and S-waves while B to the crosstalk energy. The ACC-filtered data is shown in Fig. 2.20(c). Even though some residual crosstalk energy (B) still remains, the filter has successfully eliminated most of the crosstalk energy and enhanced the continuity and coherency of the two signals modes (E and F).

2.5 Concluding Remarks

Ultrasonic PA systems have been widely used in NDT industries and medical health care. The system has the ability to use multiple elements to steer, focus and scan beams. For guided wave application in bone, these benefits of a PA system should be exploited to reduce the acquisition time and mechanical movements arising for the use of single-element transducer. However, crosstalk between elements in an array probe produces noise or artifacts, which negatively affect the data integrity and quality and lead to wrong interpretation, and should be removed.

In this work, we have applied adaptive noise cancellation in the $\tau - p$ domain

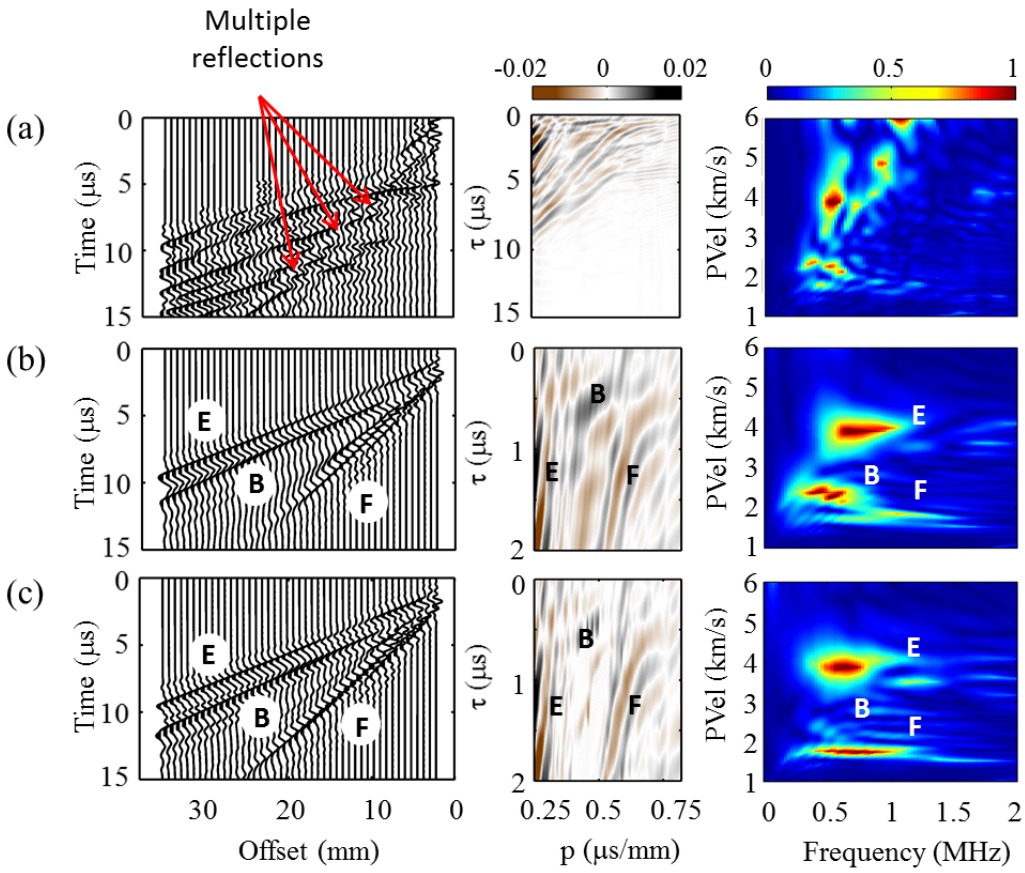

Figure 2.20: Crosstalk removal for the 6-mm bovine bone plate: (a) the original data, (b) the data after multiple reflections are muted in the $\tau - p$ domain, and (c) the ACC-filtered signal.

to reduce crosstalk artifacts in ultrasound data. The adaptive noise cancellation technique has been investigated in the time domain, but the effectiveness of the technique in the $\tau - p$ domain has not been studied. The $\tau - p$ transform is able to separate wavefields based on their intercept-time and slowness, thus rendering an effective filtering technique to eliminate undesired wave modes if necessary. Our results using Plexiglas and bone data have demonstrated that the Radon-based ACC is more reliable in removing crosstalk and recovering the crosstalk-free signals than the conventional ACC techniques in the $t - x$

domain or the normal subtraction in the $\tau - p$ domain.

Chapter 3

Excitation of Guided Waves by Beam Steering Using Two Array Probes*

Guided modes are dispersive and might come close together, posing a challenge for their identification. The ability to isolate the guided modes of interest is key for a successful analysis of ultrasound data. Post-acquisition signal processing techniques such as singular value decomposition (Sasso et al., 2006), τ-p transform (Tran et al., 2013a), group velocity filtering (Moilanen et al., 2006), dispersion compensation (Xu et al., 2012), and the joint approximate diagonalization of eigen-matrices algorithm (Song et al., 2011) are viable methods to separate wavefields. Guided modes can also be selectively excited by using angled beams.

Preferential modal excitation and selectivity using angled beams is widely used in ultrasonic NDT and material characterization (Lowe and Cawley, 1994; Wilcox et al., 2001; Rose, 2002; Luo and Rose, 2004). It is generally assumed that given the compressional wave velocity of the angled wedge and an incident angle, only a phase velocity is generated via Snell's law. However in practice,

*Part of the work in this chapter has been accepted for publication in a special issue in Ultrasonics in 2013 (Nguyen et al., 2013).

the ultrasound beam has a finite beam size and does not generate just a single phase velocity for a given wedge angle. The element size of the transducer and the incident angle influence the excitation of the GWs within the structure, which is generally known as the source influence (Ditri and Rose, 1994; Rose, 2004b; Luo and Rose, 2004). Instead of being excited with a definitive phase velocity (single excitation), GWs with a spectrum of phase velocities are generated at oblique incidence. For normal incidence, the phase velocity spectrum is very broad and dispersive, which implies infinite phase velocities to be excited, thus making mode isolation difficult. For a fixed size transducer, increasing the beam angle decreases the width of the phase velocity spectrum, thus generating fewer guided modes.

The use of angled beams to study long bone is very limited. Le et al. (2010a) used a 51° angled beam to study bulk waves at receivers deployed downstream from the point of excitation. Ta et al. (2006, 2009) used various angled beams to excite low-order longitudinal modes and was the first to mention briefly the concept of a phase velocity spectrum in the bone community without much detail. Although a pair of transducers is still the most common means to acquire bone data, ultrasound array systems have been used in axial transmission bone study (Sasso et al., 2006; Minonzio et al., 2010b, 2011b). The array system or multi-transmitter-multi-receiver system has many advantages over a single-transmitter-single-receiver system. The former has better resolution because of the smaller element footprint, fast acquisition speed, accurate coordination of the receivers, and less motion-related problems. If the system is a PA system, beam steering is possible.

In this study, we investigate the excitation of Lamb waves in plates by beam steering using two array probes. The use of two array probes: one as a

transmitter and the other as a receiver, avoids the crosstalk problem commonly seen in a single array probe as discussed in Chapter 2. Also, the adjustable spacing between the two probes allows the buildup of guided waves in longer propagation distances.

3.1 Materials and Methods

3.1.1 Preparation of Samples

We performed experiments on a brass plate and a bovine bone plate. The brass plate was 6.3 mm thick with a 255 mm $\times$ 115 mm surface dimension. We prepared a bone plate from a fresh bovine tibia. The skin and soft tissue were removed. Using a table bandsaw, both ends of the tibia were cut and then the diaphysis was cut along the axial direction to make a plate. Both surfaces of the plate were sanded and smoothed by a disk sander. The resultant bone plate had a relatively flat (190 mm $\times$ 48 mm) surface area with a thickness of approximately 6.5 mm (Fig. 3.1b). The top face was polished further to prepare the surface ready for the placement of the probes.

Figure 3.1: The 6.5-mm thick bovine bone plate.

3.1.2 Data Acquisition

We used an Olympus TomoScan FOCUS LT^{TM} Ultrasound PA system (Olympus NDT Inc., Canada) with two array probes as shown in Fig. 3.2a. The two array probes used are the 16-element (2.25L16) and 64-element (2.25L64) array probes with a central frequency of 2.25-MHz (Fig. 3.2b). Here we denote them as P16 and P64 respectively. The two probes sat tightly within a housing, which was designed and built in house to ensure the probes were stabilized and the relative distance between them were fixed during data acquisition. The active areas of the P16 and the P64 probes are respectively 12mm $\times$ 12mm and 48mm $\times$ 12mm. Both have the same pitch of 0.75mm. The two probes were connected to the scanner via a splitter.

The data were acquired using an axial transmission configuration. The experiment setup is schematically shown in Fig. 3.3, very similar to the setup for a single array probe in Fig. 2.2. The setup shows the arrangement of two probes (within housing) on ultrasound coupling media, which were in contact with the underlying plate. The plate was a brass plate or a bone plate in our case. Two pieces of 5-mm thick ultrasound gel pad, acting as coupling medium, were cut from a commercial ultrasound gel pad (Aquaflex, Parker Laboratories, Inc., USA) with surface areas slightly larger so that the probes rested comfortably on the pads. The whole set up was held in place by 3M^{TM} transpose medical tape. The ultrasound gel (Aquasonic 100, Parker Laboratories, Inc., USA) was applied to all contact surfaces to ensure good coupling. The experiments were performed at a room temperature of 22°C.

We chose to use five transducer elements as a group due to the compromise between maximum steering angle and frame size (number of acquired A-scan).

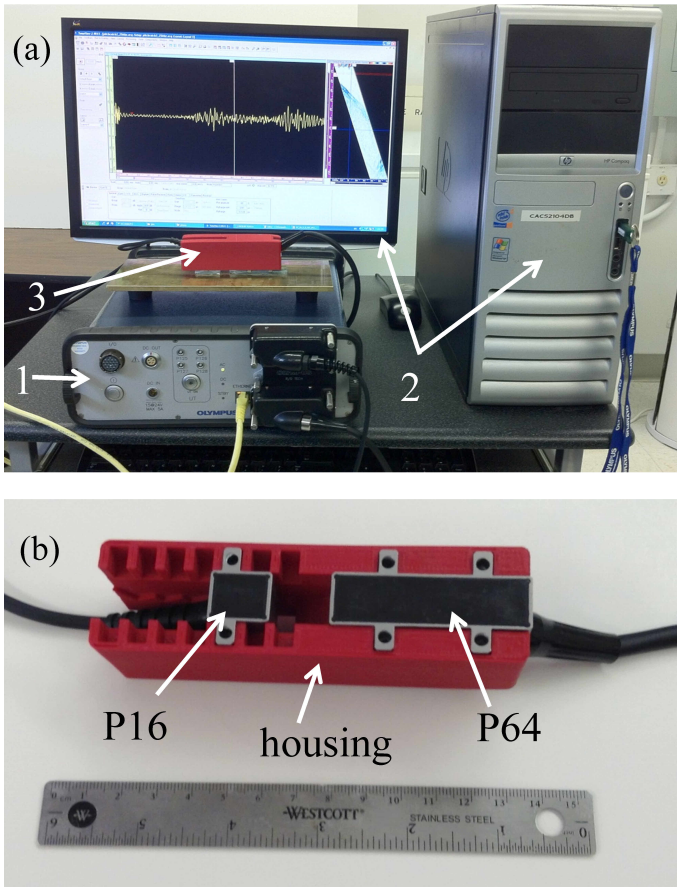

Figure 3.2: The ultrasound phased array system: (a) The TomoScan FOCUS LT^{TM} phased array acquisition system (1), the Windows XP-based computer with the TomoView^{TM} software to control the acquisition process (2), and the probe unit (3). (b) The housing with the 16-element and 64-element probes. The P16 was the transmitter array while the P64 was the receiver array.

The first five elements of the P16 probe were used as the transmitter. For the receivers, five elements worked as a group and each group was spaced by one pitch (0.75 mm) increment, that is, 1-2-3-4-5, 2-3-4-5-6, etc. The offset spanned from 22.75 mm to 67 mm with an aperture of 44.25 mm. The scanner had an option to select, within limitation, a source pulse of different dominant period, thus controlling the central frequency of the incident pulse. We chose a pulse with 1.6 MHz central frequency to compromise between resolution and

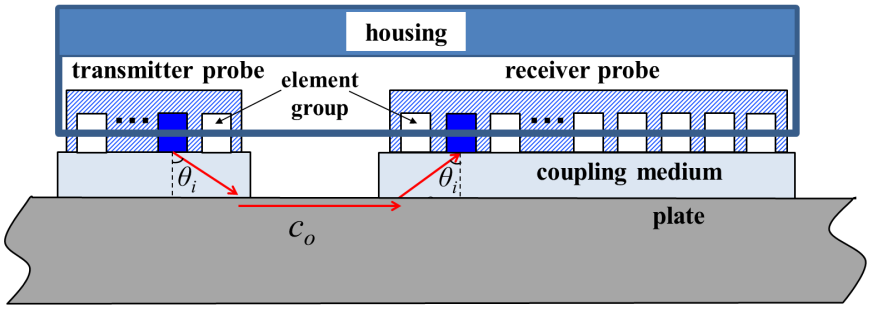

Figure 3.3: A cross-section of the experiment setup. The housing hosted two ultrasound probes in place: a 16-element (P16) probe as the transmitter and a 64-element probe as the receiver. The probes rested on the ultrasound gel pads, which acted as coupling media. The pads then overlaid the plate. Only one group (five elements) in P16 was used as source generator and 60 groups in P64 as receivers. The receivers were steered at the same inclination as the transmitting beam to enhance the receiving sensitivities to propagating guided waves with phase velocity, c_o related to the inclination, θ_i by Snell's law, $\sin\theta_i = v_w/c_o$ where v_w was the velocity of the coupling medium.

GW generation. The calculated near field length, L was around 3.7 mm, as given by $L = kA^2f/4v$ (Eq. (2.1)), where the transmitter aperture, A is 3.75 mm for a five-element source; the frequency, f is 1.6 MHz; v is 1500 m/s, the sound velocity in the ultrasound gel pad. The axial resolution of the beam was 0.24 mm based on one-half of the pulse length (Eq. (2.2)). There were 60 A-scans and each A-scan was 2500-points long with a sampling interval of 0.02 μs. The data filled a 60 $\times$ 2500 time-offset $(t - x)$ matrix of amplitudes. In our experiments, we steered both the transmitter and receiver in sync at six angles: 0° (normal incidence), 20°, 30°, 40°, 50°, and 60°. The synchronization at the same inclination enhanced the sensitivity of the receivers to record the guided waves traveling at the phase velocity of interest (Wilcox et al., 2001). Depending on the steering angle, the calculated lateral resolution ranged from 0.23 mm to 0.78 mm (Eq. (2.3)). The beam was steered at an incident angle and thus we use the terms, steering angle and incident angle, interchangeably.

3.2 Source Influence Theory: Excitation Function

When an ultrasound beam is incident on a bone surface at an angle, θ_i, a guided wave traveling with a phase velocity, c_o, between the transmitter and receiver and along the bone structure (parallel to the interface within the bone structure) will be generated according to Snell's law (Fig. 3.3):

$$\theta_i = \sin^{-1}\left(\frac{v_w}{c_o}\right) \tag{3.1}$$

or

$$k_o = k_w \sin\theta_i = \frac{\omega \sin\theta_i}{v_w} \tag{3.2}$$

where v_w is the ultrasonic velocity of the coupling medium, $k_w = \omega/v_w$ is the incident wavenumber in the coupling medium, $k_o = \omega/c_o$ is the horizontal wavenumber of the guided wave in the cortex, and ω is the radial frequency. Based on Eq. (3.1) or (3.2), only phases with a single phase velocity or wavenumber are generated, which corresponds to a horizontal excitation line at c_o for all frequencies in the $f-c$ dispersion map. However, we observed more phase velocities in our experimental data and thus Snell's law is not adequate to explain the phenomenon.

Based on the SIT (Ditri and Rose, 1994; Rose, 2004b), there exists an excitation zone where guided waves traveling with phase velocities around c_o are excited. The phase velocity spectrum is mainly governed by the size of the transducer element and the incident angle and can be approximated by the excitation function F for a piston-type source of width, A (Rose, 2004b), as

$$F(f,c) = \frac{\sigma_o |R(\theta_i)|}{2(k-k_o)} \sin\left(\frac{A(k-k_o)}{2\cos\theta_i}\right) \tag{3.3}$$

or

$$F(f,c) = \frac{A\sigma_o|R(\theta_i)|}{4\cos\theta_i}\mathrm{sinc}\,(X) \tag{3.4}$$

and

$$X = \frac{A(k-k_o)}{2\cos\theta_i} \tag{3.5}$$

where $k = \omega/c$ and σ_o is the uniform pressure on the source surface. The factor $|R(\theta_i)|$ accounts for the change in traction at the interface and more detail about this factor is referred to Ditri and Rose (1994) and Rose (2004b). In our work, we assumed σ_o and $|R(\theta_i)|$ take the values of unity and A=3.75 mm for a five-element source. For the six steering angles we used 1.6 MHz as the central frequency of the incident pulse. Their excitation spectra are shown in Fig. 3.4. We also followed Ditri and Rose (1994) to define a -9 dB phase velocity bandwidth, $\sigma_{-9\mathrm{dB}}$, for the source array:

$$\sigma_{-9\mathrm{dB}} = \frac{c_o^+ - c_o^-}{c_o} = \frac{(\Delta c_o)_{-9\mathrm{dB}}}{c_o} \tag{3.6}$$

where c_o^- and c_o^+ are the phase velocities smaller and larger than c_o respectively when $|F|$ drops by -9 dB of the maximum.

3.3 Results and Discussion

3.3.1 Brass Plate

Prior to dispersion analysis, the acquired $t-x$ data underwent some simple but essential signal processing steps. First, the triggers were muted. Second, the mean amplitude was subtracted from the data to remove the background. There was insignificant energy beyond 1.0 MHz and the data were band-pass filtered with a trapezoidal window (0.1, 0.15, 0.9, 1.0 MHz). Instead of using high resolution RT, we used the adjoint RT. We found that the adjoint solution was adequate enough for the work reported in this chapter.

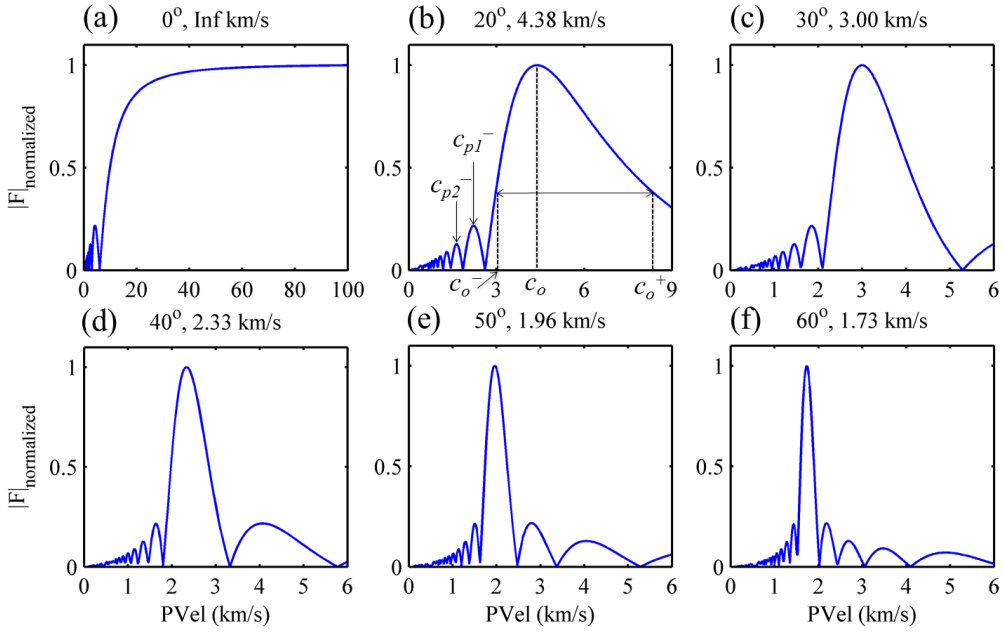

Figure 3.4: The normalized excitation spectra for six different steering angles. The velocity value shown above each figure is the phase velocity determined by Snell's law (Eq. (3.1) in the text). The phase velocity determined by Snell's law is denoted by c_o; The phase velocities, c_o^- and c_o^+, are defined at the values of $|F|$ equal to -9 dB of the maximum; The c_{p1}^- and c_{p2}^- refer to the phase velocities ($< c_o$) of the peaks of the first and second sidelobes.

Fig. 3.5 shows the $t - x$ data for six incident angles 0° (normal incidence), 20°, 30°, 40°, 50°, and 60°. The 0° data shows two distinct groups of arrivals: a high-speed group traveling approximately at 7.6 km/s and a slow-speed arrivals traveling at around 2 km/s. At 20°, the speed of the high-speed arrivals drops to 3.8 km/s while the slow-speed arrivals remain the same speed. As the steering angle increases, the high-speed arrivals decrease in amplitude and eventually fade off. At angles $> 20°$, the slow-speed arrivals persist and travel at the same 20 km/s.

Fig. 3.6 shows the Radon panels or dispersion panels of the brass plate for the six steering angles: 0° (normal incidence), 20°, 30°, 40°, 50°, and 60°.

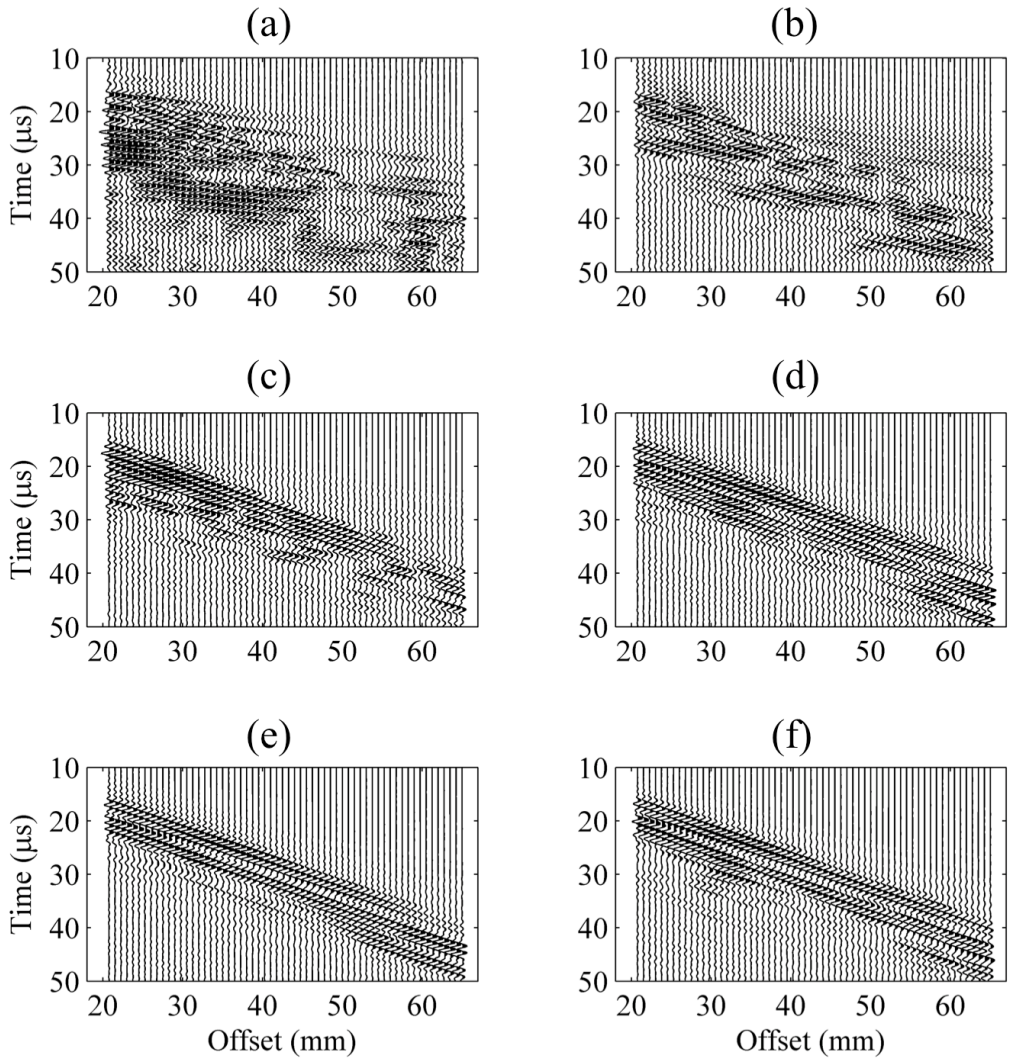

Figure 3.5: The time-offset data for the brass plate at six different incident angles: (a) 0°, (b) 20°, (c) 30°, (d) 40°, (e) 50°, and (f) 60°.

Also indicated on the figures are the excited phase velocities, c_o, as predicted by Snell's law (Eq. (3.1)) given the corresponding steering angles. We also superimposed the theoretical dispersion curves of the Lamb modes on the figure. We used the commercial DISPERSE software (Pavlakvic and Lowe, 2000) to simulate the dispersion curves based on an elastic plate model. The material properties of the brass plate are listed in Table 1. Before we discuss

each case in detail, several general observations can be made when the steering angle changes from normal incidence to 60°. First, the excitation does not generate GWs of mono phase velocity as predicted by Snell's law. Instead a spectrum of phase velocities is excited. Second, as the steering angle increases, less high-velocity GWs are excited and more low-velocity GWs are generated and focused. Third, the phase velocity spectrum becomes smaller and more selective as the steering angle increases.

Table 3.1: Parameters used to simulate dispersion curves for the brass plate and bone plate. The compressional wave velocity (v_p) and shear wave velocity (v_s) of the brass plate were taken from Table A-2 of Olympus NDT (2010) while the density (ρ) was measured. The v_p, v_s, and ρ of the bone plate were taken from Dodd et al. (2006) while the attenuation coefficients, α_p and α_p were from Le et al. (2010a). We also measured the v_p of the brass and bone plates and the measurements were 4.56 km/s and 4.09 km/s respectively, which are very close to the the reported values in the literature (Olympus NDT, 2010; Dodd et al., 2006).

Sample	brass plate	bone plate
Thickness (mm)	6.3	6.5
v_p (km/s)	4.43	4.0
v_s (km/s)	2.12	1.8
ρ (kg/m^3)	8440	1850
α_p (dB/MHz·cm)		5.0
α_s (dB/MHz·cm)		11

As shown in Fig. 3.6a, the normal beam lacks the focusing power and gives rise to a wide spectrum of GW energies of all frequencies. The normal beam excites more energetic high-velocity GWs than the low-velocity GWs. The first three antisymmetric A-modes (A_0, A_1, and A_2) and the first four symmetric S-modes (S_0, S_1, S_2, and S_3) can be identified. The majority of the energies lies above 4 km/s and between 0.5 MHz and 0.9 MHz. The three

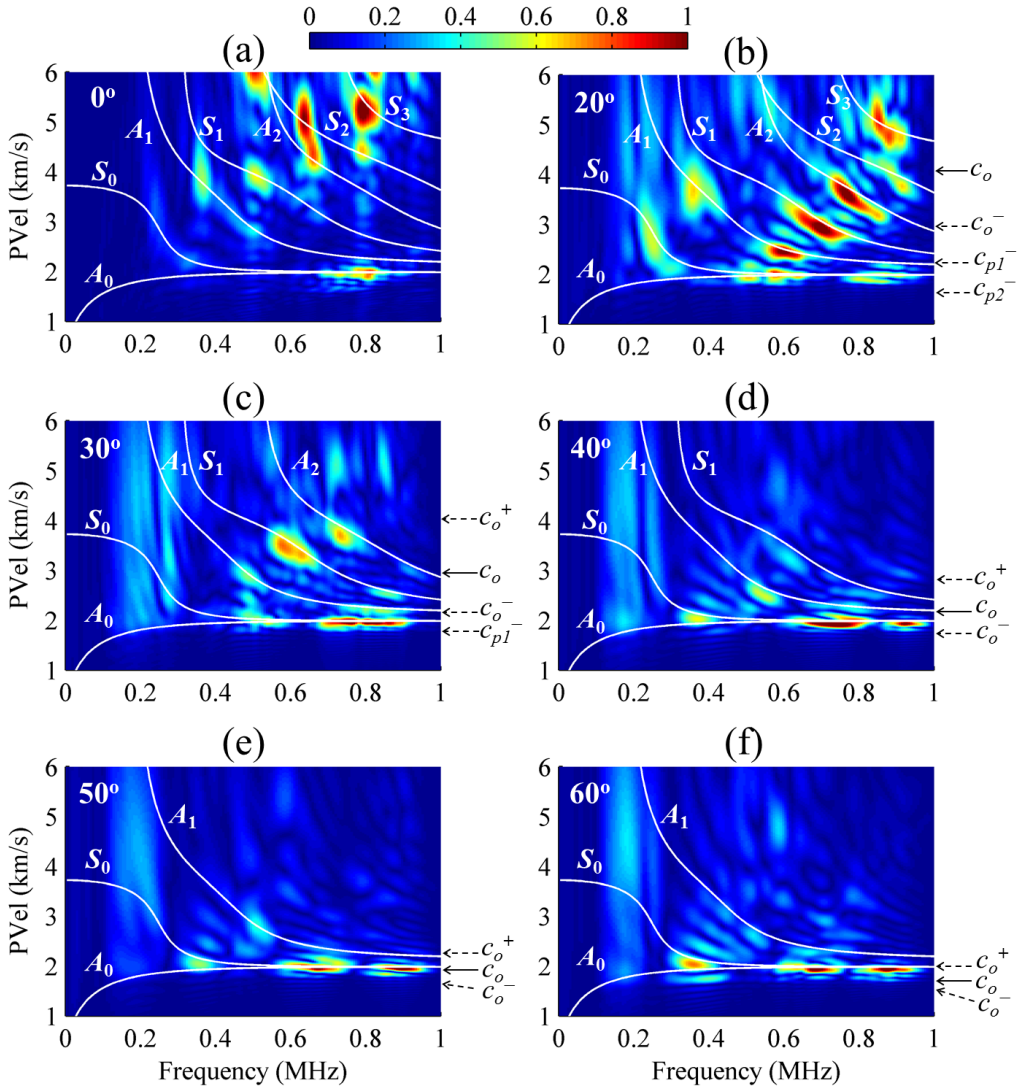

Figure 3.6: The dispersion panels of the brass plate data for the six different steering angles: (a) 0°, (b) 20°, (c) 30°, (d) 40°, (e) 50°, and (f) 60°. Superimposed are the theoretical dispersion curves. The c_o, c_o^-, c_o^+, c_{p1}^-, and c_{p2}^- are referred to Fig. 3.4 for their definitions.

strongest modes are A_2, S_2 and S_3. The low-velocity GW energies are very weak. The beam excites the higher frequency portion of the low-order modes A_0 and S_0 at 0.8 MHz where they converge into a small energy cluster around 1.95 km/s. At 0°, the Snell's law-predicted phase velocity is a very large value

or, theoretically speaking, infinity, indicating that the high-velocity GWs are favorably excited. It is quite challenging to identify and isolate guided modes using normal beam excitation. At 20° incidence (Fig. 3.6b), the beam excites guided waves around the predicted phase velocity of 4.38 km/s. All seven previously-identified guided modes are present but their cluster peaks show up at different (higher) frequencies. The low-velocity GWs below 4.38 km/s are energetic. The beam excites strong S_0 energy around 0.2 MHz and beyond. However above 0.4 MHz, the dispersion curves of the A_0 and S_0 come together and it is difficult to tell which mode the energy clusters between 0.5 and 0.8 MHz belong to. When the steering angle increases to 30° (Fig. 3.6c), the predicted phase velocity is 3.0 km/s. The number of GW modes, especially the high-velocity modes above 4.0 km/s, decreases and the low-velocity modes around 1.95 km/s are more enhanced. At this angle, we only identify five significant modes, A_0, S_0, A_1, S_1, and A_2 with the majority of the GW energies lying between 0.4 and 0.9 MHz. For the A_0, S_0, A_1, and S_1, the simulated dispersion curves match very well with the corresponding modal clusters with the curves going through the first two low-order modal clusters on their tracks. It is interesting to note from these dispersion curves that the same modal energies are not continuous on their respective dispersion curves. This might imply that the modes experience strong attenuation at certain frequencies. The first two low-order modes consistently show their presence between 0.5 MHz - 0.9 MHz with progressively stronger energies than those at smaller steering angles. The last three modes start to lose their strength as the steering angle increases. The weakening of the A_1 mode is obvious. When the steering angle increases from 40° (Fig. 3.6d) to 60° (Fig. 3.6f), the predicted imaged phase velocities drops from 2.33 km/s to 1.73 km/s and all high-velocity GWs

become less visible. Only two low-velocity A_0 and S_0 modes exist and are imaged with enhanced focus and resolution. In addition, more energy is excited at frequencies lower than 0.4 MHz. At 60° incidence, there is some 0.4 MHz energy traveling around 1.8 km/s, which seems to belong to the A_0 mode. Overall, the dispersion curves match the excited Lamb modes reasonably well.

3.3.2 Bovine Bone Plate

We investigated further the guided mode selectivity and focusing by beam-steering on a bovine bone plate. The data was processed using the same procedures and parameters as those for the brass plate data.

Fig. 3.7 shows the $t - x$ data for six incident angles. Similarly to the brass data, the 0° data shows two distinct groups of arrivals: a high-speed group traveling approximately at 5.4 km/s and a slow-speed arrivals traveling at around 2 km/s. At 20°, the speed of the high-speed arrivals drops to 3.4 km/s while the slow-speed arrivals remain the same speed. As the steering angle increases, the high-speed arrivals decrease in amplitude and eventually fade off. At angles $> 20°$, the slow-speed arrivals persist and travel at the same 20 km/s.

The dispersion panels (Fig. 3.8) show the same general observations as those in the brass plate. Notably, the ultrasound beam energizes a spectrum of phase velocities and at smaller steering angles, the beam favors the excitation of high-velocity GWs. As the steering angle is more oblique, the spectrum is narrower and the beam is more selective toward low-velocity excitation.

The predicted phase velocities, c_o, for the six steering angles remain the same as those for brass plate (Table 2). The normal beam excites a wide spectrum of phase velocities with an emphasis on high-velocity GWs (Fig. 3.8a).

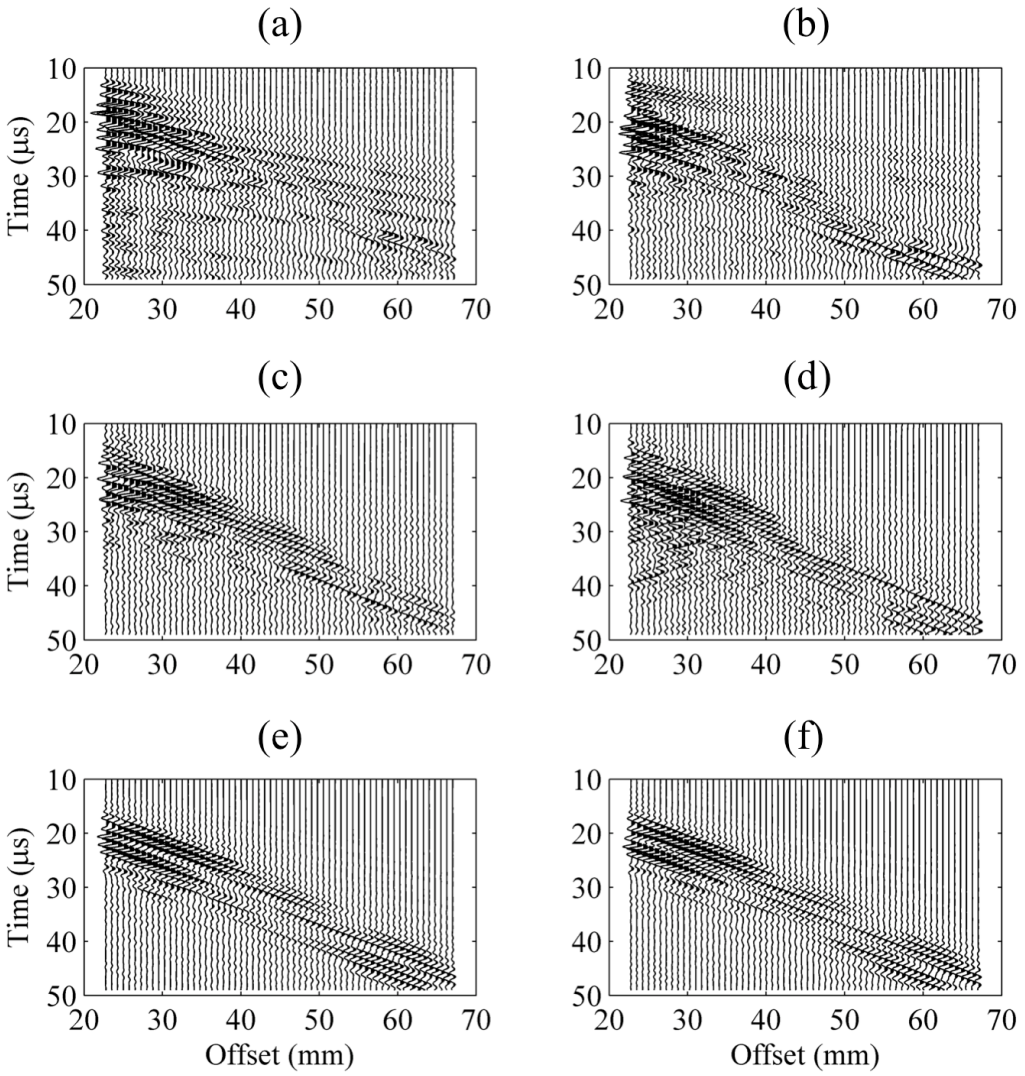

Figure 3.7: The time-offset data for the bone plate at six different incident angles: (a) 0°, (b) 20°, (c) 30°, (d) 40°, (e) 50°, and (f) 60°.

The energetic GWs travel at velocities above 3.5 km/s. There are a few weak and small energy clusters. We calculated the dispersion curves using a plate model with absorption (Table 1). The match is not perfect with some clusters lying between dispersion curves. We managed to identify eight Lamb modes: 4 antisymmetric modes, A_0-A_3 and 4 symmetric modes, S_0-S_3. The

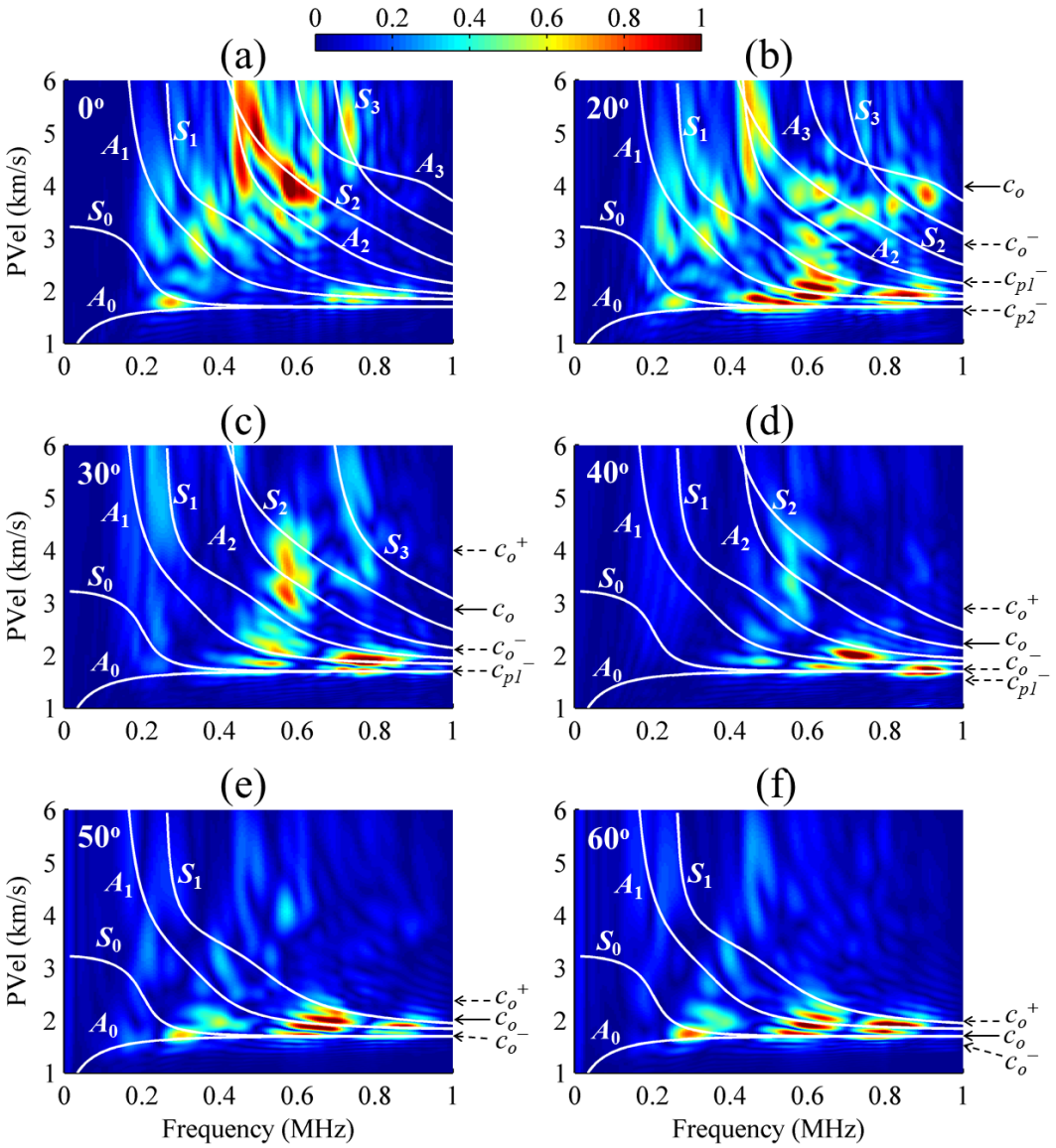

Figure 3.8: The dispersion panels of the bone plate data for six different steering angles: (a) 0°, (b) 20°, (c) 30°, (d) 40°, (e) 50°, and (f) 60°. Superimposed are the theoretical dispersion curves. The c_o, c_o^-, c_o^+, c_{p1}^-, and c_{p2}^- are referred to Fig. 3.4 for their definitions.

two high-intensity clusters are the fast-traveling A_2 and S_2 modes. The A_1 curve goes through a low-frequency cluster (∼0.32 MHz) and a high-frequency cluster (∼0.75 MHz). In the neighborhood of 1.9 km/s, there is a noticeable

fragmented band of weak energies at 0.25 MHz and between 0.7 and 0.8 MHz, which is better imaged in the 20° panel (Fig. 3.8b). Except for the A_3 mode, which is absent in the brass plate dispersion panel, the modes in the brass plate and bone plate are very similar with A_2 and S_2 being the two strongest modes. As the steering increases, the low-velocity energies receive enhanced focusing and imaging resolution while the high-velocity phases become weaker, e.g.,the A_2 and S_2 modes. At 30° (Fig. 3.8c), only GWs traveling below 4.2 km/s are energized. As the steering angle increases from 30° (Fig. 3.8c) to 60° (Fig. 3.8f), only the bundle of GW energies bounded between A_0 and S_1 and over 0.5 MHz is imaged while the rest of the GWs lose their intensity and become hardly visible. At 50° (Fig. 3.8e) and 60° (Fig. 3.8f), this band of low-order energies experiences enhanced excitation. It is worth mentioning here that the adjoint RT is able to resolve these closely packed energy clusters. The steered beam greatly enhances and focuses the slow-traveling (around 1.75 km/s) small energy cluster around 0.3 MHz, which lie between the A_0 and S_0. Quite similar to the brass plate, the A_0 and S_0 modes persist in all steering angles.

3.3.3 Excitation Function

The SIT predicts that the loading size of the transducer influences the range of phase velocities generated by the transmitting source (Ditri and Rose, 1994; Rose, 2004b). For a given angle of incidence, the beam does not generate a single phase velocity (based on Snell's law) but a spectrum of phase velocities. The GW modes with dispersion curves passing through the phase velocity zones for a given frequency have greater "chance" to be excited as compared to the portion of the curves, which are far from the zone. This

excitation probability is provided by the excitation function defined by Eq. (3.7). However, the strength of the excitation at that particular frequency is governed by the excitability function of the theory. As shown in the results, even though the dispersion curves of the modes run through the -9 dB phase velocity bandwidth, the modal energies are sporadic and not continuous along the dispersion tracks. It is uncertain whether the absence of some frequency components is due to the attenuation of those components or the preferential modal excitation at certain frequencies. Studying the excitability function is beyond the scope of this study. Here, we attempt to use the excitation function of the source influence theory to explain the observed behaviors of the dispersion energies with steering angles.

The -9 dB bandwidth defines a range of phase velocities within which significant excitation may happen. The bandwidth parameters are tabulated in Table 2. An example of how to delineate the bandwidth of a spectrum and other relevant parameters is provided by the 20° case in Fig. 3.4b. As shown in Fig. 3.4, the normal beam excitation function exceeds the -9 dB value over an "infinitely" wide phase velocity range and there is basically no selectivity to phase velocity. This is evident in both data sets (Fig. 3.6a and Fig. 3.8a). The selectivity to phase velocities improves when the steering angle increases. The bandwidth decreases from 128% to 21% of c_o when the incident angle increases from 20° to 60°, offering enhanced modal selectivity. The bandwidth-narrowing, as predicted by the excitation function, is supported by our experimental data. While the the upper boundary of the observed GW region is well defined by c_o^+, the lower boundary of the region is less so by the c_o^-. For the two largest steering angles, 50° (Fig. 3.6e and Fig. 3.8e) and 60° (Fig. 3.6f and Fig. 3.8f), the c_o^- and c_o^+ are the lower and upper boundaries

of the observed phase velocity spectra. For the brass plate, the c_o^- and c_o^+ are sufficient to define the 40° phase velocity spectrum (Fig. 3.6d). However the c_{p1}^- and c_{p2}^- are required to define the lower bounds of the observed phase velocity regions for the 30° (Fig. 3.6c) and 20° (Fig. 3.6b) respectively. For the bone plate, the c_{p1}^- fixes the lower bounds of the 30° (Fig. 3.8c) and 40° (Fig. 3.8d) while the c_{p2}^- outlines the lower bound for the 20° (Fig. 3.8b). Although the -9 dB bandwidth defines the dominant phase velocity region where the excitation may happen, the excitation can happen in the sidelobes of the excitation function as illustrated by the dispersion panels of the experiment data.

Table 3.2: Parameters for the -9 dB phase velocity bandwidth for five steering angles. The c_{p1}^- and c_{p2}^- refer to the phase velocities ($< c_o$) of the peaks of the first and second sidelobes.

θ_i	c_o (km/s)	c_o^+ (km/s)	c_o^- (km/s)	$(\Delta c_o)_{-9\text{dB}}$ (km/s)	$\sigma_{-9\text{dB}}$	c_{p1}^- (km/s)	c_{p2}^- (km/s)
20°	4.38	8.54	2.95	5.59	1.28	2.22	1.62
30°	3.00	4.32	2.29	2.03	0.68	1.84	1.44
40°	2.33	2.95	1.93	1.02	0.44	1.62	1.34
50°	1.96	2.30	1.71	0.59	0.30	1.50	1.30
60°	1.73	1.93	1.57	0.36	0.21	1.42	1.27

3.4 Concluding Remarks

In this study, we investigated the use of a commercial non-medical PA system to excite GWs within a brass plate and a bone plate with two array probes. Acquisition with two probes not only eliminated the crosstalk between transducer elements but also allowed an adjustable long offset for GW buildup. By using fixed 5 elements of a 16-element probe as the loading and a 64-element receiver probe, many energetic fast and slow GWs of a wide frequency range

were excited and observed in both plates. We also studied the effects of modal selectivity within the plates by beam-steering. The results show that 0° excitation generated many modes with no modal discrimination and the oblique beam excited a spectrum of phase velocities spread asymmetrically about c_o. The width of the excitation region decreased as the steering angle increased, rendering modal selectivity at large angles. The phenomena were well predicted by the excitation function of the source influence theory. The low-order modes were better imaged at steering angles $\geq 30°$ for both plates. By varying the angle of the steered beam, the excited bandwidth of the phase velocity spectrum changed, in good agreement with the prediction by the excitation function of the source influence theory. Consequently, modal selectivity is possible by choosing larger steering angles.

The study has also demonstrated the feasibility of using the two-probes PA system for future *in vivo* study. The results of this study allow us to consider a PA system for clinical work. The acquisition time by a PA system is reduced significantly by 100 fold without any mechanical probe movement as compared to a single-transmitter-single-receiver system and problems relating to the inaccurate recording transducer's coordination, patient discomfort, and patient motion are minimized if used in clinical settings. The low-order low-velocity GW modes have been consistently observed in both plates. The adjoint RT has successfully extracted the dispersion energies with good resolution. Using the PA system in combination with low frequency toneburst for *in vivo* study will be the next avenue for future studies.

Chapter 4

Conclusions and future directions

QUS uses mechanical waves to probe the bone tissues and has great potential to characterize the geometrical and mechanical properties of bone. GWs are generated by the interaction of elastic waves within the boundaries of the cortex and able to travel long distances interacting with the cortex. Cortices of long bones are good waveguides to support the propagation of ultrasonic GWs. Therefore, GWs are capable of providing more information about the cortex than bulk waves.

Ultrasonic GWs in long bone have been investigated mostly using a pair of angled beam transducers with wedges. In this thesis, we attempted to use a commercial, non-medical Olympus TomoScan FOCUS LT$^{\text{TM}}$ ultrasound PA system to study long bones. The study was progressively performed by first using a single array probe and then two array probes.

There was an issue with crosstalk for the single array probe. We have applied the conventional ACC in the Radon or $\tau - p$ domain and have found that the filter was very effective to reduce the crosstalk and recover the signals. The crosstalk, which differs with the signals in time-intercept and slowness, can be

filtered effectively. The results using experimental data have showed that the Radon-based ACC performs much better than the conventional ACC, which operates in the time-space domain. The results have verified our hypothesis that the crosstalk can be filtered using an adaptive algorithm.

We next considered beam steering with two array probes. Acquisition with two probes not only eliminated the crosstalk between transducer elements but also allowed adjustable long offset for GW buildup. Using brass and bone plates, we steered the beam for six different incident angles and found the excited phase velocity spectrum was in good agreement with the prediction by the excitation function from the source influence theory. Modal selectivity is possible by choosing larger steering angle. As the steering angle increases, low-velocity guided modes are preferentially excited. Our second hypothesis that the guided modes can be preferentially excited is also justified.

Our study so far has shown promising application of an ultrasound PA system for clinical work. The acquisition time will be greatly reduced and patient comfort will be enhanced significantly. Also, problems relating to patient movement during acquisition will be reduced, which improves data quality. Using the PA system in combination with low frequency toneburst for *in vivo* studies will be the next direction for future studies.

To illustrate the complexity of an *in vivo* problem, Fig. 4.1 shows the dispersion panels of a human tibia data set for five different steering angles (0°, 20°, 30°, 40°, and 60°). The volunteer was a 50-year old male subject. The data were influenced by many unknown factors such as overlying soft tissue, inhomogeneity of the bone tissues, anisotropy, uneven cortical thickness, bone curvature, to name a few. Identifying the guided modes in the data is a challenging task. Similar to the *in vitro* data, the same observations can

be made. The 0° beam generated many modes with no selectivity. As the steering angle increased, more low-velocity guided modes were preferentially excited, excluding the high-velocity guided modes. In order to advance our work toward clinical application, we need to have a good understanding of ultrasound interaction with soft-tissue/bone system. Therefore, *in vitro* and *in vivo* studies to investigate the effect of soft-tissue and its thickness variation on the guided modes will be a project of our interest.

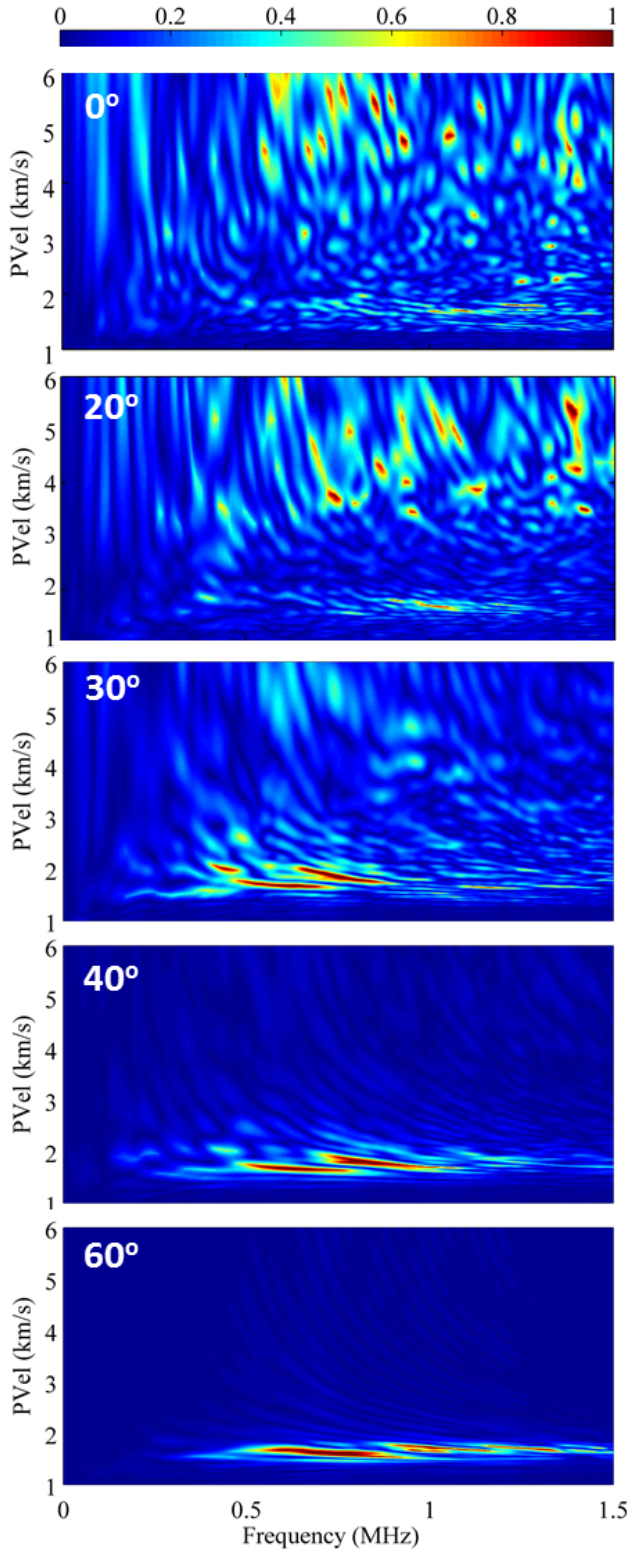

Figure 4.1: The dispersion panels of a human tibia data set for five different incident angles: 0°, 20°, 30°, 40°, and 60°.

Bibliography

Augat, P., Reeb, H., and Claes, L. (1996). Prediction of fracture load at different skeletal sites by geometric properties of the cortical shell. *Journal of Bone and Mineral Research*, 11(9):1356–1363.

Baer, R. L. and Kino, G. S. (1984). Theory for cross coupling in ultrasonic transducer arrays. *Applied Physics Letters*, 44(10):954–956.

Barnett, E. and Nordin, B. (1960). The radiological diagnosis of osteoporosis: a new approach. *Clinical Radiology*, 11(3):166–174.

Bartl, R. and Frisch, B. (2009). *Osteoporosis [electronic Book]: Diagnosis, Prevention, Therapy*. Springer.

Blake, G. M., Wahner, H. W., and Fogelman, I. (1999). *The evaluation of osteoporosis: dual energy X-ray absorptiometry and ultrasound in clinical practice*. CRC Press.

Bloom, R. A. (1980). A comparative estimation of the combined cortical thickness of various bone sites. *Skeletal Radiology*, 5(3):167–170.

Bossy, E., Talmant, M., Defontaine, M., Patat, F., and Laugier, P. (2004a). Bidirectional axial transmission can improve accuracy and precision of ultrasonic velocity measurement in cortical bone: a validation on test materials. *IEEE Transactions on Ultrasonics, Ferroelectrics and Frequency Control*, 51(1):71 –79.

Bossy, E., Talmant, M., Peyrin, F., Akrout, L., Cloetens, P., and Laugier, P. (2004b). An in vitro study of the ultrasonic axial transmission technique at the radius: 1-mhz velocity measurements are sensitive to both mineralization and intracortical porosity. *Journal of Bone and Mineral Research*, 19(9):1548–1556.

Bousson, V., Meunier, A., Bergot, C., Vicaut, É., Rocha, M. A., Morais, M. H., Laval-Jeantet, A.-M., and Laredo, J.-D. (2001). Distribution of intracortical porosity in human midfemoral cortex by age and gender. *Journal of Bone and Mineral Research*, 16(7):1308–1317.

Brady, C., Arbona, J., In Soo, A., and Yufeng, L. (2012). Fpga-based adaptive noise cancellation for ultrasonic nde application. In *2012 IEEE International Conference on Electro/Information Technology (EIT)*, pages 1–5.

Bushberg, J. T. and Boone, J. M. (2011). *The essential physics of medical imaging*, chapter 16. Lippincott Williams & Wilkins.

Cameron, J. R. and Sorenson, J. (1963). Measurement of bone mineral in vivo: an improved method. *Science*, 142(3589):230–232.

Cheeke, J. (2002). *Fundamentals and applications of ultrasonic waves*. CRC Press, New York.

Chen, J., Foiret, J., Minonzio, J.-G., Talmant, M., Su, Z., Cheng, L., and Laugier, P. (2012a). Measurement of guided mode wavenumbers in soft tissue–bone mimicking phantoms using ultrasonic axial transmission. *Physics in Medicine & Biology*, 57(10):3025.

Chen, W., Le, L. H., and Lou, E. H. M. (2012b). Ultrasound imaging of spinal vertebrae to study scoliosis. *Open Journal of Acoustics*, 2(3):95–103.

Claerbout, J. F. (2004). *Earth soundings analysis: Processing versus inversion*, chapter 5. Boston: Blackwell Scientific Publications.

Dalgaard, E., Auken, E., and Larsen, J. (2012). Adaptive noise cancelling of multichannel magnetic resonance sounding signals. *Geophysical Journal International*, 191(1):88–100.

Ditri, J. and Rose, J. (1994). Excitation of guided waves in generally anisotropic layers using finite sources. *Journal of Applied Mechanics*, 61(2):330–338.

Dodd, S., Cunningham, J., Miles, A., Gheduzzi, S., and Humphrey, V. (2006). Ultrasonic propagation in cortical bone mimics. *Physics in Medicine & Biology*, 51(18):4635.

Engl, H. W. and Grever, W. (1994). Using the L–curve for determining optimal regularization parameters. *Numerische Mathematik*, 69(1):25–31.

Gerlanc, M., Haddad, D., Hyatt, G. W., Langloh, J. T., and Hilaire, P. S. (1975). Ultrasonic study of normal and fractured bone. *Clinical Orthopaedics and Related Research*, 111:175–180.

Gruber, M., Bauer, J., Dobritz, M., Beer, A., Wolf, P., Woertler, K., Rummeny, E., and Baum, T. (2013). Bone mineral density measurements of the proximal femur from routine contrast-enhanced mdct data sets correlate with dual-energy x-ray absorptiometry. *European Radiology*, 23(2):505–512.

Gu, Y. J. and Sacchi, M. (2009). Radon transform methods and their applications in mapping mantle reflectivity structure. *Surveys in geophysics*, 30(4-5):327–354.

Haney, M. and OBrien, W. (1986). Temperature dependency of ultrasonic propagation properties in biological materials. *Tissue Characterization with Ultrasound. CRC Press, Boca Raton, Fla.*

Hansen, P. C. (1992). Analysis of discrete ill-posed problems by means of the l-curve. *SIAM Review*, 34(4):561–580.

Haykin, S. (1996). *Adaptive Filter Theory*, chapter 9.Least-Mean-Square Algorithm, page 437. Prentice Hall, 3rd edition.

Hien, V. T. T., Khan, N. C., Lam, N. T., Le, D. N., Nhung, B. T., Nakamori, M., Kunii, D., Sakai, T., Yamamoto, S., et al. (2005). Determining the prevalence of osteoporosis and related factors using quantitative ultrasound in vietnamese adult women. *American Journal of Epidemiology*, 161(9):824–830.

INNOVATE R&D (2013). Osteoporosis. `http://www.educatehealth.ca/patient/bones-and-joints/osteoporosis.aspx`. [Online] Accessed: 21/04/2013.

International Osteoporosis Foundation (2013). Facts and statistics. `http://www.iofbonehealth.org/facts-statistics`. [Online] Accessed: 01/06/2013.

IvyRose Holistic (2013). The Structure and Functions of Bones. `http://www.ivy-rose.co.uk/HumanBody/Skeletal/Skeletal_System.php`. [Online] Accessed: 21/04/2013.

Ji, Q., Le, L. H., Filipow, L. J., and Jackson, S. A. (1998). Ultrasonic wave propagation in water-saturated aluminum foams. *Ultrasonics*, 36(6):759–765.

Kelly, T. L., Crane, G., and Baran, D. T. (1994). Single X-Ray absorptiometry of the forearm - precision, correlation, and reference data. *Calcified Tissue International*, 54(3):212–218.

Kilappa, V., Xu, K., Moilanen, P., Heikkola, E., Ta, D., and Timonen, J. (2013). Assessment of the fundamental flexural guided wave in cortical bone by an ultrasonic axial-transmission array transducer. *Ultrasound in Medicine & Biology*.

Kino, G. S. and DeSilets, C. S. (1979). Design of slotted transducer arrays with matched backings. *Ultrasonic Imaging*, 1(3):189 – 209.

Krueger, D., Fidler, E., Libber, J., Aubry-Rozier, B., Hans, D., and Binkley, N. (2013). Spine trabecular bone score subsequent to bone mineral density improves fracture discrimination in women. *Journal of Clinical Densitometry*.

Langton, C. M. and Njeh, C. F. (2003). *The physical measurement of bone*, chapter 1, pages 20–21. Taylor & Francis.

Langton, C. M. and Njeh, C. F. (2010). *The physical measurement of bone*. CRC Press.

Langton, C. M., Palmer, S. B., and Porter, R. W. (1984). The measurement of broadband ultrasonic attenuation in cancellous bone. *Engineering in Medicine*, 13(2):89–91.

Le, L. H. (1998). An investigation of pulse-timing techniques for broadband ultrasonic velocity determination in cancellous bone: a simulation study. *Physics in Medicine & Biology*, 43(8):2295–2308.

Le, L. H., Gu, Y. J., Li, Y., and Zhang, C. (2010a). Probing long bones with ultrasonic body waves. *Applied Physics Letters*, 96:114102.

Le, L. H., Zhang, C., Ta, D., and Lou, E. H. M. (2010b). Measurement of tortuosity in aluminum foams using airborne ultrasound. *Ultrasonics*, 50(1):1–5.

Lee, K. I. and Choi, M. J. (2007). Phase velocity and normalized broadband ultrasonic attenuation in polyacetal cuboid bone-mimicking phantoms. *The Journal of the Acoustical Society of America*, 121(6):EL263–EL269.

Lee, K. I. and Yoon, S. W. (2012). Correlations between ultrasonic guided wave velocities and bone properties in bovine tibia in vitro. *Journal of the Acoustical Society of America*, 131(5):EL375–EL381.

Li, M. and Hayward, G. (2011). Ultrasound nondestructive evaluation (nde) imaging with transducer arrays and adaptive processing. *Sensors*, 12(1):42–54.

Link, T. M., Majumdar, S., Augat, P., Lin, J. C., Newitt, D., Lu, Y., Lane, N. E., and Genant, H. K. (1998). In vivo high resolution mri of the calcaneus: differences in trabecular structure in osteoporosis patients. *Journal of Bone and Mineral Research*, 13(7):1175–1182.

Louis, O., Willnecker, J., Soykens, S., Van den Winke, P., and Osteaux, M. (1995). Cortical thickness assessed by peripheral quantitative computed tomography: accuracy evaluated on radius specimens. *Osteoporosis International*, 5(6):446–449.

Lowe, M. and Cawley, P. (1994). The applicability of plate wave techniques for the inspection of adhesive and diffusion bonded joints. *Journal of Nondestructive Evaluation*, 13(4):185–200.

Lowe, M. J. S. (2002). *Encyclopedia of vibration*, volume 11, chapter Guided waves in structures. Academic Press.

Lowet, G. and VanderPerre, G. (1996). Ultrasound velocity measurement in long bones: Measurement method and simulation of ultrasound wave propagation. *Journal of Biomechanics*, 29(10):1255–1262.

Luo, W. and Rose, J. L. (2004). Lamb wave thickness measurement potential with angle beam and normal beam excitation. *Materials Evaluation*, 62(8):860–866.

Majumdar, S., Newitt, D., Mathur, A., Osman, D., Gies, A., Chiu, E., Lotz, J., Kinney, J., and Genant, H. (1996). Magnetic resonance imaging of trabecular bone structure in the distal radius: Relationship with X-ray tomographic microscopy and biomechanics. *Osteoporosis International*, 6(5):376–385.

Mather, J., MacDermid, J. C., Faber, K. J., and Athwal, G. S. (2013). Proximal humerus cortical bone thickness correlates with bone mineral density and can clinically rule out osteoporosis. *Journal of Shoulder and Elbow Surgery*, 22(6):732–738.

Meyer, U., Ernst, D., Zahner, L., Schindler, C., Puder, J. J., Kraenzlin, M., Rizzoli, R., and Kriemler, S. (2013). 3-year follow-up results of bone mineral content and density after a school-based physical activity randomized intervention trial. *Bone*.

Minonzio, J.-G., Foiret, J., Talmant, M., and Laugier, P. (2010a). Measurement of guided mode wave numbers in anisotropic absorbing material: Application to cortical bone evaluation. *2010 IEEE Ultrasonics Symposium (IUS)*, pages 2159–2162.

Minonzio, J.-G., Foiret, J., Talmant, M., and Laugier, P. (2011a). Impact of attenuation on guided mode wavenumber measurement in axial transmission on bone mimicking plates. *The Journal of the Acoustical Society of America*, 130(6):3574–3582.

Minonzio, J.-G., Talmant, M., and Laugier, P. (2010b). Guided wave phase velocity measurement using multi-emitter and multi-receiver arrays in the axial transmission configuration. *The Journal of the Acoustical Society of America*, 127(5):2913–2919.

Minonzio, J.-G., Talmant, M., and Laugier, P. (2011b). Measurement of guided mode wave vectors by analysis of the transfer matrix obtained with multi-emitters and multi-receivers in contact. *Journal of Physics: Conference Series*, 269(1):012003.

Miyabara, Y., Holmes III, D., Camp, J., Miller, V., and Kearns, A. (2012). Comparison of calibrated and uncalibrated bone mineral density by ct to dexa in menopausal women. *Climacteric*, 15(4):374–381.

Moilanen, P., Määttä, M., Kilappa, V., Xu, L., Nicholson, P., Alén, M., Timonen, J., Jämsä, T., and Cheng, S. (2013). Discrimination of fractures by low-frequency axial transmission ultrasound in postmenopausal females. *Osteoporosis International*, 24(2):723–730.

Moilanen, P., Nicholson, P., Kärkkäinen, T., Wang, Q., Timonen, J., and Cheng, S. (2003). Assessment of the tibia using ultrasonic guided waves in pubertal girls. *Osteoporosis International*, 14(12):1020–1027.

Moilanen, P., Nicholson, P., Kilappa, V., Cheng, S., and Timonen, J. (2006). Measuring guided waves in long bones: Modeling and experiments in free and immersed plates. *Ultrasound in Medicine & Biology*, 32(5):709–719.

Moilanen, P., Nicholson, P. H., Kilappa, V., Cheng, S., and Timonen, J. (2007). Assessment of the cortical bone thickness using ultrasonic guided waves: Modelling and in vitro study. *Ultrasound in Medicine & Biology*, 33(2):254 – 262.

Muller, M., Moilanen, P., Bossy, E., Nicholson, P., Kilappa, V., Timonen, J., Talmant, M., Cheng, S., and Laugier, P. (2005). Comparison of three ultrasonic axial transmission methods for bone assessment. *Ultrasound in Medicine & Biology*, 31(5):633–642.

Müller, R. and Rüegsegger, P. (1996). Analysis of mechanical properties of cancellous bone under conditions of simulated bone atrophy. *Journal of Biomechanics*, 29(8):1053–1060.

Nguyen, T. K. C., Le, L. H., Tran, T. N. H. T., and Lou, E. H. M. (2013). Excitation of ultrasonic lamb waves using a phased array system with two array probes: Phantom and in-vitro bone studies. *Ultrasonics*. **In press**.

Nicholson, P. H., Moilanen, P., Kärkkäinen, T., Timonen, J., and Cheng, S. (2002). Guided ultrasonic waves in long bones: modelling, experiment and in vivo application. *Physiological Measurement*, 23(4):755–768.

Nishiyama, K. K., Macdonald, H. M., Buie, H. R., Hanley, D. A., and Boyd, S. K. (2010). Postmenopausal women with osteopenia have higher cortical porosity and thinner cortices at the distal radius and tibia than women with normal abmd: An in vivo hr-pqct study. *Journal of Bone and Mineral Research*, 25(4):882–890.

Njeh, C. F. (1999). *Quantitative ultrasound: assessment of osteoporosis and bone status*, chapter 1, page 3. CRC Press.

Olympus NDT (2007). Advances in Phased Array Ultrasonic Technology Applications. pp.85–87.

Olympus NDT (2010). Phased Array Testing: Basic Theory for Industrial Applications.

Osteoporosis Canada (2013). Capture the fracture. `http://www.osteoporosis.ca/about-osteoporosis-canada/`. [Online] Accessed: 22/04/2013.

Pavlakvic, B. and Lowe, M. (2000). DISPERSE: An interactive program for generating dispersion curves (Version 2.0.16i). Imperial College, London UK.

Perilli, E., Briggs, A. M., Kantor, S., Codrington, J., Wark, J. D., Parkinson, I. H., and Fazzalari, N. L. (2012). Failure strength of human vertebrae: prediction using bone mineral density measured by dxa and bone volume by micro-ct. *Bone*, 50(6):1416–1425.

Protopappas, V. C., Fotiadis, D. I., and Malizos, K. N. (2006). Guided ultrasound wave propagation in intact and healing long bones. *Ultrasound in Medicine & Biology*, 32(5):693–708.

Rose, J. L. (2002). A baseline and vision of ultrasonic guided wave inspection potential. *ASME Journal of Pressure Vessel Technology*, 124(3):273–282.

Rose, J. L. (2004a). Ultrasonic guided waves in structural health monitoring. *Key Engineering Materials*, 270:14–21.

Rose, J. L. (2004b). *Ultrasonic waves in solid media*. Cambridge university press.

Sacchi, M. D. (1997). Reweighting strategies in seismic deconvolution. *Geophysical Journal International*, 129(3):651–656.

Sachse, W. and Pao, Y.-H. (1978). On the determination of phase and group velocities of dispersive waves in solids. *Journal of applied Physics*, 49(8):4320–4327.

Sasso, M., Talmant, M., Haiat, G., Laugier, P., and Naili, S. (2006). Development of a multi-dimensional svd based technique for multi-receivers ultrasound used in bone status characterization. In *Sensor Array and Multichannel Processing, 2006. Fourth IEEE Workshop on*, pages 663–666. IEEE.

Sasso, M., Talmant, M., Haiat, G., Naili, S., and Laugier, P. (2009). Analysis of the most energetic late arrival in axially transmitted signals in cortical bone. *Ultrasonics, Ferroelectrics and Frequency Control, IEEE Transactions on*, 56(11):2463–2470.

Sayed, A. (2003). *Fundamentals of adaptive filtering*. Hoboken, New Jersey: John Wiley& Sons.

Scales, J. A., Gersztenkorn, A., and Treitel, S. (1988). Fast l_p solution of large, sparse, linear systems: Application to seismic travel time tomography. *Journal of Computational Physics*, 75(2):314–333.

Siegel, I., Anast, G., and Fields, T. (1958). The Determination Of Fracture Healing By Measurement Of Sound Velocity Across The Fracture Site. *Surgery Gynecology & Obstetrics*, 107(3):327–332.

Song, X., Ta, D., and Wang, W. (2011). Analysis of superimposed ultrasonic guided waves in long bones by the joint approximate diagonalization of eigen-matrices algorithm. *Ultrasound in Medicine & Biology*, 37(10):1704–1713.

Ta, D., Huang, K., Wang, W., Wang, Y., and Le, L. H. (2006). Identification and analysis of multimode guided waves in tibia cortical bone. *Ultrasonics*, 44:279–284.

Ta, D., Wang, W., Wang, Y., Le, L. H., and Zhou, Y. (2009). Measurement of the dispersion and attenuation of cylindrical ultrasonic guided waves in long bone. *Ultrasound in Medicine & Biology*, 35(4):641–652.

Talmant, M., Kolta, S., Roux, C., Haguenauer, D., Vedel, I., Cassou, B., Bossy, E., and Laugier, P. (2009). In vivo performance evaluation of bi-directional ultrasonic axial transmission for cortical bone assessment. *Ultrasound in Medicine & Biology*, 35(6):912–919.

TCHS Sports Medicine ROP (2013). Classification of Bone by Shape. `http://sportsmed.drkennethmartin.com/images/bonecat.jpg`. [Online] Accessed: 01/06/2013.

The Altanta Equine Clinic (2013). Bone Sequestrum Formation. `http://www.atlantaequine.com/pages/client_lib_sequestrum.html`. [Online] Accessed: 21/04/2013.

Tran, T. N. H. T., Le, L. H., Sacchi, M. D., Nguyen, V. H., and Lou, E. H. M. (2013a). Application of $\tau - p$ transform to filter and reconstruct multi channel ultrasonic guided-wave fields. In *Proceedings of the 5th European Symposium on Ultrasonic Charaterization of Bone (ESUCB), Granada, Spain May 7-10, 2013*, pages 102–103.

Tran, T. N. H. T., Stieglitzb, L., Le, L. H., and Gu, Y. J. (2013b). Analysis of ultrasonic waves propagating in a bone plate over a water half-space with and without overlying soft tissue. *Ultrasound in Medicine & Biology*. **In press**.

Turner, C. (2002). Biomechanics of bone: determinants of skeletal fragility and bone quality. *Osteoporosis International*, 13(2):97–104.

Turner, G. (1990). Aliasing in the tau-p transform and the removal of spatially aliased coherent noise. *Geophysics*, 55(11):1496–1503.

Vieth, V., Link, T. M., Lotter, A., Persigehl, T., Newitt, D., Heindel, W., Majumdar, S., et al. (2001). Does the trabecular bone structure depicted by high-resolution mri of the calcaneus reflect the true bone structure? *Investigative Radiology*, 36(4):210–217.

Viktorov, I. A. (1967). *Rayleigh and Lamb waves: physical theory and applications*, volume 147. Plenum press New York.

Wear, K. (2000). The effects of frequency-dependent attenuation and dispersion on sound speed measurements: Applications in human trabecular bone. *IEEE Transactions on Ultrasonics, Ferroelectrics, and Frequency Control*, 47(1):265–273.

Wenzel, S. W. (1992). *Applications of ultrasonic lamb waves*. PhD thesis, University of California, Berkeley.

Werner, P. (2005). Knowledge about osteoporosis: assessment, correlates and outcomes. *Osteoporosis International*, 16(2):115–127.

WHO Scientific Group (2004). *Prevention and management of osteoporosis*. Geneva: World Health Organization.

Widrow, B., Glover Jr, J. R., McCool, J. M., Kaunitz, J., Williams, C. S., Hearn, R. H., Zeidler, J. R., Dong Jr, E., and Goodlin, R. C. (1975). Adaptive noise cancelling: Principles and applications. *Proceedings of the IEEE*, 63(12):1692–1716.

Wilcox, P., Lowe, M., and Cawley, P. (2001). Mode and transducer selection for long range lamb wave inspection. *Journal of Intelligent Material Systems and Structures*, 12(8):553–565.

Wirnitzer, B., Grimm, W., Schmidt, H., and Klinnert, R. (1998). Interference cancelation in ultrasonic sensor arrays by stochastic coding and adaptive filtering. In *Proceedings of the IEEE International Conference on Intelligent Vehicles*.

Xu, K., Ta, D., Moilanen, P., and Wang, W. (2012). Mode separation of lamb waves based on dispersion compensation method. *Journal of the Acoustical Society of America*, 131:2714–2722.

Zebaze, R., Ghasem-Zadeh, A., Bohte, A., Iuliano-Burns, S., Mirams, M., Price, R. I., Mackie, E. J., and Seeman, E. (2010). Intracortical remodelling and porosity in the distal radius and post-mortem femurs of women: a cross-sectional study. *Lancet*, 375(9727):1729–1736.

Zhang, C., Le, L. H., Zheng, R., Ta, D., and Lou, E. H. M. (2011). Measurements of ultrasonic phase velocities and attenuation of slow waves in cellular aluminum foams as cancellous bone-mimicking phantoms. *The Journal of the Acoustical Society of America*, 129:3317.

Zhang, R., Ta, D., Liu, C., and Chen, C. (2013). Feasibility of bone assessment with ultrasonic backscatter signals in neonates. *Ultrasound in Medicine & Biology*.

Zheng, R., Le, L., Sacchi, M., and Lou, E. H. M. (2009). Broadband ultrasound attenuation measurement of long bone using peak frequency of the echoes. *IEEE Transactions on Ultrasonics, Ferroelectrics and Frequency Control*, 56(2):396 –399.

Zhou, S. W., Wojcik, G. L., and Hossack, J. A. (2003). An approach for reducing adjacent element crosstalk in ultrasound arrays. *IEEE Transactions on Ultrasonics, Ferroelectrics, and Frequency Control*, 50(12):1752–1761.

Appendix A

Effective Aperture Angle

Consider the isosceles triangle, $\triangle ABC$ where $AB = d$, the height h, and the steering angle, α are given. We measure the following lengths

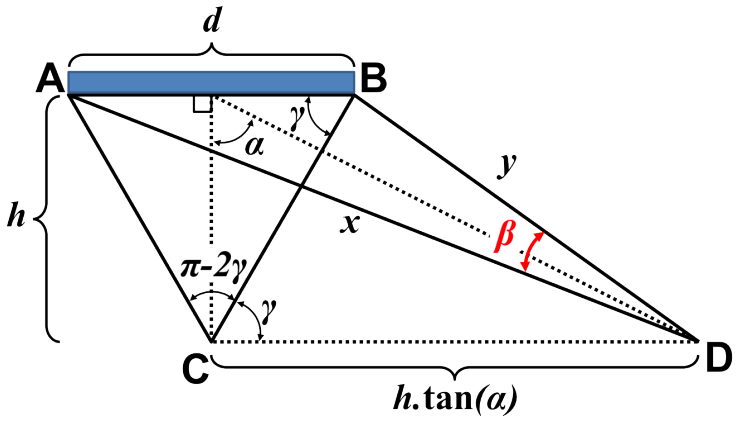

Figure A.1: Diagram used to determine the effective aperture angle, β. AB represents the aperture of a group of elements used as emitter.

$$l_{CD} = h \tan \alpha \tag{A.1}$$

and

$$l_{AC} = l_{BC} = \sqrt{\frac{d^2}{4} + h^2}. \tag{A.2}$$

Using Eq. (A.2), the angle $\angle ABC$, denoted by γ, is

$$\cos\gamma = \frac{(d/2)}{l_{BC}} = \frac{(d/2)}{\sqrt{d^2/4 + h^2}} \tag{A.3}$$

and

$$\cos(\pi - \gamma) = -\cos\gamma = -\frac{(d/2)}{\sqrt{d^2/4 + h^2}}. \tag{A.4}$$

For the triangle $\triangle BCD$, we have

$$l_{BC}^2 + l_{CD}^2 - 2l_{BC}l_{CD}\cos\gamma = l_{BD}^2 \tag{A.5}$$

and, by substituting Eq. (A.1), (A.2), and (A.3),

$$\begin{aligned} l_{BD} &= \sqrt{l_{BC}^2 + l_{CD}^2 - 2l_{BC}l_{CD}\cos\gamma} \\ &= \sqrt{\frac{d^2}{4} + \frac{h^2}{\cos^2\alpha} - dh\tan\alpha}. \end{aligned} \tag{A.6}$$

Similarly for the triangle $\triangle ACD$, we have

$$l_{AC}^2 + l_{CD}^2 - 2l_{AC}l_{CD}\cos(\pi - \gamma) = l_{AD}^2 \tag{A.7}$$

and substituting Eq. (A.1), (A.2), and (A.4) yields

$$\begin{aligned} l_{AD} &= \sqrt{l_{AC}^2 + l_{CD}^2 - 2l_{AC}l_{CD}\cos(\pi - \gamma)} \\ &= \sqrt{\frac{d^2}{4} + \frac{h^2}{\cos^2\alpha} + dh\tan\alpha} \end{aligned} \tag{A.8}$$

For the triangle $\triangle ABD$, we have

$$l_{AD}^2 + l_{BD}^2 - 2l_{AD}l_{BD}\cos\beta = l_{AB}^2 \tag{A.9}$$

and, making use of Eq. (A.6) and (A.8), we get

$$\begin{aligned} \cos\beta &= \frac{l_{AD}^2 + l_{BD}^2 - d^2}{2xy} \\ &= \frac{2h^2/\cos^2\alpha - d^2/2}{2\sqrt{(d^2/4 + h^2/\cos^2\alpha)^2 - d^2h^2\tan^2\alpha}}. \end{aligned} \tag{A.10}$$

From Eq. (A.10), β can be determined by

$$\beta = \arccos\left[\frac{2h^2/\cos^2\alpha - d^2/2}{2\sqrt{(d^2/4 + h^2/\cos^2\alpha)^2 - d^2h^2\tan^2\alpha}}\right]. \tag{A.11}$$